
CSI-NET: UNIFIED BODY CHARACTERIZATION AND ACTION RECOGNITION

Fei Wang*

Xi'an Jiaotong University &
Carnegie Mellon University
feiwang@cmu.edu

Jinsong Han

Xi'an Jiaotong University &
Zhejiang University
hanjinsong@gmail.com

Shiyuan Zhang

Xi'an Jiaotong University
shiyangzhang932@gmail.com

Xu He

Xi'an Jiaotong University
hexu.xjtu@gmail.com

Dong Huang

Carnegie Mellon University
donghuang@cmu.edu

ABSTRACT

Channel State Information (CSI) of WiFi signals becomes increasingly attractive in human sensing applications due to the pervasiveness of WiFi, robustness to illumination and view points, and little privacy concern comparing to cameras. In majority of existing works, CSI sequences are analyzed by traditional signal processing approaches. These approaches rely on strictly imposed assumption on propagation paths, reflection and attenuation of signal interacting with human bodies and indoor background. This makes existing approaches very difficult to model the delicate body characteristics and activities in the real applications. To address these issues, we build CSI-Net, a unified Deep Neural Network (DNN), that fully utilizes the strength of deep feature representation and the power of existing DNN architectures for CSI-based human sensing problems. Using CSI-Net, we jointly solved two body characterization problems: biometrics estimation (including body fat, muscle, water and bone rates) and human identification. We also demonstrated the application of CSI-Net on two distinctive action recognition tasks: the hand sign recognition (fine-scaled action of the hand) and falling detection (coarse-scaled motion of the body). Besides the technical contribution of CSI-Net, we present major discoveries and insights on how the multi-frequency CSI signals are encoded and processed in DNNs, which, to the best of our knowledge, is the first attempt that bridges the WiFi sensing and deep learning in human sensing problems. *Codes is available at <https://github.com/geekfew/CSI-Net>*

Keywords channel state information · mobile human sensing · deep learning

1 Introduction

Recent years witness rapid growth of techniques using Channel State Information (CSI) of WiFi signals in sensing human bodies. These techniques lead to major boost of applications in human-computer interaction [1, 2, 3], health care[4, 5, 6, 7] and surveillance[8, 9, 10]. Comparing to computer vision based human sensing, WiFi-based techniques enable non-line-of-sight activity recognition[10], allow prevalent deployment in daily living and working environment, and arises little privacy concern.

The core problem of WiFi sensing is to prepare a proper representation of signals that directly correlates with human body characteristics and activities. Existing work used hand-crafted features:(1) Temporally aligned CSI sequences by Dynamic Time Wrapping (DTW)[11, 12, 13, 14, 3, 15]. (2) Statistical features of the CSI sequences, such as the average, variance, and entropy. It is unclear how to manually design person-specific features for body characteristics and person-invariant features for activities. Moreover, the interaction of WiFi signals with human body and background results in complex multi-path transmission, reflection and attenuation of CSI, making it extremely difficult for hand-craft feature to extract delicate information from CSI data.

*Work done when at the Robotics Institute, CMU

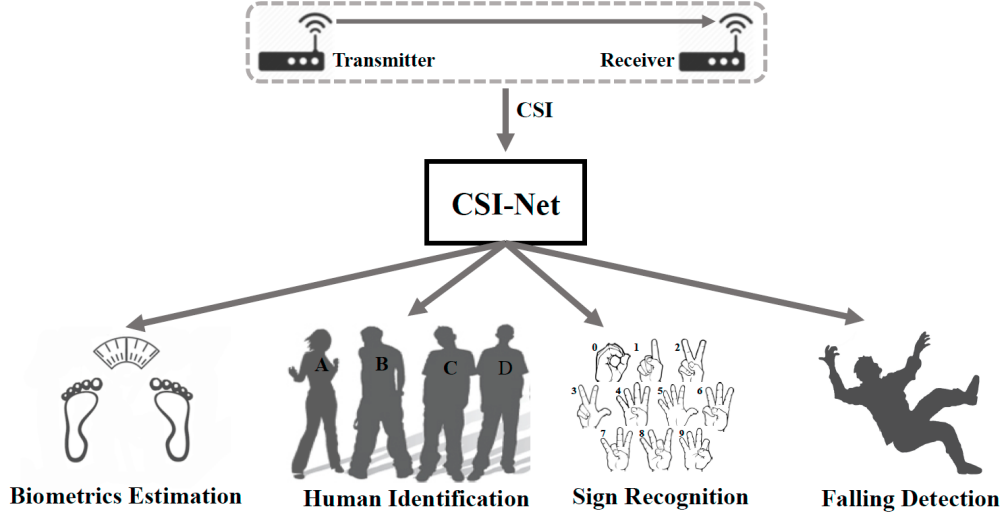


Figure 1: System overview. CSI is generated from the transmitter/receiver WiFi communication. CSI-Net is a unified body characterization and activity recognition deep learning architecture. In this paper, we apply CSI-Net to do body characterization tasks such as biometrics estimation and human identification, meanwhile, we also apply it to do activity recognition tasks such as hand sign recognition and falling detection.

On the other hand, recent advances of deep learning exhibit extraordinary ability in learning data representation from data. There are some preliminary attempts on indoor localization[16] and human identification[17]. However, to our knowledge, no existing work has built a unified deep learning framework that solves multiple WiFi sensing problems. To build this framework, three main challenges need to be addressed: **1.** How to adapt CSI sequences for convolution computation in DNNs. **2.** How to design DNN architectures for extracting CSI features. **3.** How to generalize DNNs to a variety of WiFi sensing tasks.

We address above issues as follows:

- 1. CSI sequences as input tensors.** Note that at each time-stamp of a CSI sequence, there are signal samples from multiple subcarriers (30 subcarriers in our paper). Each subcarrier has a distinctive frequency and interacts with human bodies. How to design the computation within and between subcarrier is the key problem to address when sending CSI sequences to a convolutional neural network. From the successful multi-channel signal models, such as Blind signal separation (BSS), the combined signals can be well-approximated as a linear combination among channels. We keep the interaction among channels while release the information within individual channels using convolution computation. Specifically, we take the 30-dimensional CSI sample at each time-stamp as a multi-channel tensor, where each channel is a 1×1 matrix and corresponds to one subcarrier.
- 2. De-convolving input tensors to spatially-encoded maps.** Successful DNNs used in computer vision tasks, such as object detection and recognition[18, 19, 20, 21, 22, 23, 24, 25], extract structured spatial information using cross-channel convolutions, in which images are decomposed into smaller multi-channel feature maps. In order to harness the power of existing DNNs, each channel of input tensor, needs to expand and encode spatial information for cross-channel convolutions. We build a *generation stage* of CSI-Net, in which *transposed convolution* layers (De-convolving) transform the CSI input tensor into spatially-coded maps. Then the spatially-coded maps are used to extract features for sensing tasks (*feature learning stage*).
- 3. Task-specific output layers.** For each sensing task, the features above are fed to *fully-connected* layers followed by classification or regression output functions.

The technical contribution of this paper can be summarized as follows.

1. We propose CSI-Net, a deep learning framework for human sensing with WiFi CSI sequences.
2. We solve a variety of human sensing tasks using CSI-Net: biometrics estimation, human identification, hand sign recognition and falling detection.
3. We qualitatively analyze the influence of human body on WiFi signals and build a database for CSI-based human sensing tasks. Based on extensive experiment results, we conclude that besides the tasks demonstrated

in the paper, many more tasks, such as retrieving the human shape and pose, can be achieved using CSI-Net and WiFi signals.

Moreover, CSI-Net is not merely a deep learning application in WiFi sensing. This paper presents major discoveries and insights on how the multi-frequency CSI signals are encoded and processed in CSI-Net. We empirically show that

1. CSI-Net learns to identify subjects by encoding body biometrics information. Jointly training CSI-Net for multiple tasks, such as biometrics estimation and human identification, can mutually facilitate these tasks.
2. CSI data is spatially-encoded in chess-board-like images in DNNs. The size of highlight points increases when number of categories decreases. The distances between different categories significantly magnified as the network depth increases.

To our knowledge this is the first attempt to visualize and analyze the process of DNNs on CSI data.

The rest of this paper is organized as follows. A brief related work is reviewed in Section 2. Section 3 describes a WiFi signal model at the presence of the human body. The framework of CSI-Net is presented detailedly at Section 4. The implementation details including the data collection/preprocessing and DNNs' architecture/training are shown at Section 5. The results of experimental evaluation and analysis of spatially-encoded maps are presented at Section 6. We present our major discoveries in Section 6.7 and discuss the limitation and potential improvement of CSI-Net at Section 7. Finally this paper is concluded in Section 8. More details are left in Appendix due to limited space.

2 Related Work

We summarize related CSI-based work on body characterization and activity recognition in this section.

2.1 Body Characterization

The majority of CSI-based body characterization work focuses on human identification [26, 27, 28, 29, 30, 31]. These work use walking pattern to identify person identity. Specifically, subjects are asked to walk along a predefined path repeatedly while the CSI sequences are recorded as training data. Then classification algorithms are developed to map the CSI data to identities. In these approaches, computing discriminative representation for each user is very difficult yet essential to the identification performance. In [27, 28, 29, 30, 31], statistical features, e.g., *maximum*, *minimum*, *mean*, *energy* and *entropy*, are extracted from the CSI sequences and fed to classifiers, e.g., Support Vector Machine(SVM), for human identification. However, calculating these metrics requires each subject to walk several meters along a predefined path, which is time-consuming and inefficient in the test phase, and limits the practical implementation. Similarly, the method in [17] collects training data when subjects walk along multiple predefined paths. Then, in the test phase, the subject can be identified while he/her only walks along one of those paths. It also verifies that person-specific CSI sequences can be discriminated for other activities, such as opening microwave oven, fetching documents, or eating at the table.

There exist two common drawbacks in above work: (1) Feature representations of CSI are manually designed, and it is difficult to guarantee that features are discriminative for human identification. (2) Subjects are required to be highly cooperative in repeating certain activities in order to register their identities. It is time consuming and error-prone to gain sufficient and well-annotated training data. In practice, it is more challenging to find highly cooperative users for these systems, such that users have to repeat certain activities many times for acceptable data quality.

In this paper, we build CSI-Net to automatically learn person-specific features from CSI data. Our CSI-Net further extends the findings in [17] that human can even be identified by only standing still. CSI-Net eliminates the tedious requirement of repeating certain activities. Because of learning person-specific features, we show that CSI-net is, to our knowledge, the first work to estimate human biometrics using WiFi signals.

2.2 Activity Recognition

There exist a wide spectrum of applications on activity recognition using WiFi signals. Besides walking, CSI sequences have been used to recognize keystroking[3, 15], breathing[7, 32] and falling[33, 5, 11]. In terms of processing flow, recent approaches in CSI-based activity recognition fall into two main schemas. **(1) Feature classification:** *raw CSI* -> *filtered CSI* -> *hand-crafted features* (statistical features)-> *classifier* -> *activity classes*. This schema uses statistical features, such as *maximum*, *minimum*, *mean*, *energy* and *entropy*, to represent variance of CSI sequences caused by body activities and train a classifier to recognize these activities. However, some researchers showed that an activity may vary in duration, speed or range even for a same subject[3], which decreases the robustness of recognition. **(2)**

Sequence matching: *raw CSI* \rightarrow *filtered CSI* \rightarrow *dynamic time wrapping (DTW)*[34] \rightarrow *k-nearest neighbors (kNN)* \rightarrow *activity prediction*. This schema directly computes the distance of CSI variance aligned by DWT and employs kNN to recognize the activities with minimal distance[14, 3, 15, 11, 12, 13]. The second schema may perform better in discriminating activities consisting of micro activities like keystroke[3]. However, to recognize an activity, the later schema requires computing distances between its corresponding CSI sequences and every training CSI sequences, which is very time-consuming. In addition, kNN algorithm is generally inferior to a supervised learning classifier, such as SVM, that learns recognition rules from CSI sequences to activity classes.

Note that it is very difficult to manually design general features that encode spatial and temporal structures of many activity classes. In this paper, we explore the extraordinary ability of DNNs in learning activity representation from CSI data, and propose an unified deep learning framework that solves multiple WiFi sensing problems. Furthermore, most of current work are to recognize activities with motion. In contrast, we extend the CSI-based activity recognition to the static case, where CSI sequences under static postures can also be recognized. To our best knowledge, our work is among the first attempts to recognize human activities from the view of human static postures.

2.3 Deep Learning on CSI

Most applications of neural networks on CSI data only used shallow networks. In [35, 16], a moving mobile device records location-specific CSI amplitudes from a fixed WiFi router. Then a neural network with 3 hidden layers were used to transform the amplitudes into the location of the mobile device. In [36, 37], CSI phases are used to locate mobile device with similar techniques. In [38], a neural network with 5 layers are used to do channel estimation in WiFi system. In [39], recurrent neural networks with long-short-time memory (LSTM)[40] cells are proposed to identify whether the transmitter and receiver is line-of-sight or not for the communication performance monitoring purpose.

Above works display the possibility and effectiveness of SHALLOW neural networks (less than 5 layers) as alternate nonlinear operators comparing to traditional optimizers, regressors or classifier. None of these work used DEEP neural networks, performed end-to-end feature extraction or solved multiple semantic tasks in an unified framework. In this paper, we carefully modified mainstream deep convolution neural network (DCNN), such as ResNet[24], to perform body characterization and activity recognition.

2.4 Bio-electromagnetics in WiFi Signal Band

Our work is based on fundamental principles in Bio-electromagnetics. Bio-electromagnetics studies the changes of electromagnetic (EM) waves when encountering biological bodies. Many literatures specifically studied the Bio-electromagnetics in WiFi Signal Band, *e.g.*, 2.4G WiFi (2470MHz-2544MHz) and 5G WiFi (5033MHz-6006MHz). In [41], dielectric parameters like permittivity and conductivity of body tissues, such as fat, muscle and liver *etc.*, were measured within the EM frequency of 10Hz to 20GHz (see details in Table 1). In [42, 43], human body is modeled as layered tissues with different dielectric parameters, as sketched in Fig. 2 (right). Specific absorption rate (SAR) of WiFi signal propagating through these layered tissues can be measured and used to characterize human body biometrics. Furthermore, standing-wave effects occur at certain fat layer thickness and frequencies within 30MHz-6000MHz. [44] also used the layered tissue model to compute the power decay and time delay of EM wave when propagating through human body at the frequency of 2.45GHz. This work provides critical cues to measure human body spatially, making it possible to capture body gestures/actions using the decayed and delayed WiFi signals.

3 Layered Tissue Model

Based on the layered tissue model in bio-eletromagnetics, we further explain how the human body, even without motions, can cause CSI variances and these variances are embedded with fine-grained human body information.

In Fig. 2 (left), we show a cross-slice image of a female body [45], where the bigger part in the middle is the torso, and two smaller parts are the arms. Looking closely in the torso part, we can see several layers of human body, such as skin, the fat under skin, muscle, the fat on the viscera, viscera, bone, *etc.* In [41], dielectric characteristics of many body tissues have been measured at the regular body temperature ($37.0^{\circ}C/98.6^{\circ}F$). The results are selectively listed in Table 1 at the EM frequency of 2.4GHz and 5GHz, *i.e.*, frequencies in the WiFi bands. In [42, 43], a human torso is considered as layered tissues with different dielectric parameters for studying the specific absorption rate on certain EM wave.

According to these works, for simplicity we sketch the layered tissue model in the context of WiFi communication systems in Fig. 2 (right), in which the human body consists of 3 layers with different thickness and dielectric properties. In the figure, human body is considered as a propagation medium of WiFi signals, and hence capable of affecting

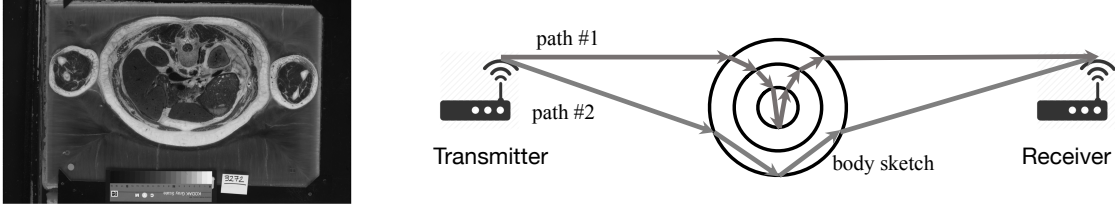


Figure 2: Wireless signals model at the presence of human body. **Left:** A cross-slice image of a female body[45], where circled layers are the skin, fat, muscle, viscus and bone. (we gray it to protect readers.) **Right:** We simplify human body as a cylinder of three layers with different dielectric properties[41]. The transmitting signals from the Transmitter interact with human body along multiple propagation paths before reaching the Receiver. Here we sketched two paths of the signals.

Tissues	Frequency	Permittivity	Conductivity (S/m)
Skin (Dry)	2.4GHz	39.81	1.78
	5GHz	33.11	3.98
Skin (Wet)	2.4GHz	39.81	2.24
	5GHz	35.48	5.62
Fat (Average Infiltrated)	2.4GHz	10.23	0.32
	5GHz	8.91	0.71
Fat (Not Infiltrated)	2.4GHz	5.62	0.1
	5GHz	5.59	0.32
Muscle	2.4GHz	50.12	2.51
	5GHz	44.67	5.62
Bone (Cortical)	2.4GHz	11.22	0.56
	5GHz	8.91	1.12
Bone (Cancellous)	2.4GHz	15.85	0.71
	5GHz	14.13	1.41

Table 1: Dielectric characteristics, permittivity and conductivity of human tissues at 2.4GHz and 5GHz WiFi band. These tissues have different dielectric characteristics in each band, which generate CSI variances in the received WiFi signals.

transmitted WiFi signals and producing WiFi variances. Before reaching the receiver, the signals from the transmitter may be reflected or refracted when propagating through body layers along multiple propagation paths. For easy illustration, we only draw two propagation paths of WiFi signals. Note that for simplicity, we ignore the influence from other objects in the environment.

Taking the path #1 (plotted in the Fig. 2 (right)) as an example, if we know the characteristics of this path, including the properties of each layer and EM frequency, we could calculate the body-information-embedded power decay and time delay when WiFi signals reaching the receiver. Next, we show how the body information is embedded into the received WiFi signals according to [44].

Formally, denote the WiFi signal emitted from the transmitter as x . The EM wave function is written as $x = Ae^{-j2\pi ft + \phi}$, where A , f and ϕ are the amplitude, frequency and initial phase, respectively. Before formulating the impacts of human body and the air on the bypassing WiFi signals, we define some notations in Table 2.

Time delay: the sum of propagation time delay in all medium. For each medium, the time delay equals to $t_i = d_i/v_i$. where v_i is the speed of WiFi signals in this propagation medium, and is computed as $v_i = 1/\sqrt{\mu_i \epsilon_i}$ [46]. For path #1, the overall time delay is

$$t = \sum_{i=1}^n d_i \sqrt{\mu_i \epsilon_i} + d_0 \sqrt{\mu_0 \epsilon_0} \quad (1)$$

where n is the number of tissue layers.

Symbols	Meaning
d_0	Distance of signals propagating through the air
d_i	Distance of signals propagating through the i^{th} layer of human body
c_0	Power decay in the air
c_i	Power decay in the i^{th} layer of human body
μ_0	Permeability of the air
μ_i	Permeability of the i^{th} layer of human body
ε_0	Permittivity of the air
ε_i	Permittivity of the i^{th} layer of human body

Table 2: List of the mathematical symbols.

Power decay: the product of power decay in all medium (Table 2). The overall power decay is computed as

$$A' = Ac_0 \prod_{i=1}^n c_i \quad (2)$$

Please refer to [44] for a more comprehensive expression, which utilizes Friis Transmission Equation[47] and Beer-Lambert Law[48] to compute power decay. Combining Eq. 1 and Eq. 2, the received WiFi signals are

$$y = \prod_{i=1}^n \underbrace{c_i e^{-j2\pi f \sum_{i=1}^n d_i \sqrt{\mu_i \varepsilon_i}}}_{\text{~~~~~}} \cdot c_0 e^{-j2\pi f d_0 \sqrt{\mu_0 \varepsilon_0}} \cdot x \quad (3)$$

Note that we mark the WiFi variation caused by the presence of human body with a wave line. From the equation, we know that the dielectric characteristics of body tissues such as thickness, permeability, permittivity *etc.*, are embedded into the received WiFi signals.

Moreover, the commercially available devices such as commodity body composition scales, *e.g.*, Mi® [49] use the impedance of human body on bypass electricity to analyze the fine-grained body information, such as the body fat/muscle/water/bone rate. Very similar to this principle, we believe the fine-grained body information embedded in WiFi signals could also be extracted. Different from the contact devices above, parsing body characteristics from WiFi signals requires powerful nonlinear mapping algorithms, *i.e.*, CSI-Net.

4 CSI-Net

As shown in Fig. 3, CSI-Net is composed of three functional components: the generation stage, the feature learning stage and the task stage. The generation stage transforms CSI data to feature maps with the spatially-encoded patterns. The feature learning stage further maps the spatially-encoded patterns to the features for sensing tasks. Finally, the features are used to produce outputs in the task stage.

In the remainder of this section, we first describe the input tensor of CSI-Net, then explain three functional components in detail.

4.1 Input Tensor of CSI-Net

CSI is computed from a channel estimation process in the 802.11 n/g WiFi system. Given a WiFi packet from a transmitter to a receiver, channel estimation is formulated as,

$$Y = HX + N \quad (4)$$

where, Y is the received data, X is the transmitted data, H is the CSI, and N is the noise of the WiFi system. Using the software tools listed in Table 3, CSI can be extracted as a complex-valued sequence, $\mathbf{A} \in \mathcal{C}^{N_{sa} \times N_{sc}}$, where N_{sa} and N_{sc} are the number of sampled WiFi packets and number of subcarriers, respectively. In our experiments, we deploy Linux 802.11n CSI Tool [50] to record CSI sequences of 30 subcarriers. Due to the unstable CSI phases, we only use CSI amplitudes as raw input data $\mathbf{A} \in \mathcal{R}^{N_{sa} \times 30}$, \mathcal{R} denotes the set of *real* numbers.

Note that, in conventional computer vision problems, input tensors of Deep Neural Networks (DNNs) are images with size of $Channel \times Height \times Width$, where $Channel$ is the number of color channels, $Height$ and $Width$ represent the image height and width, respectively. Typical RGB images have 3 channels (red, green and blue), which correspond

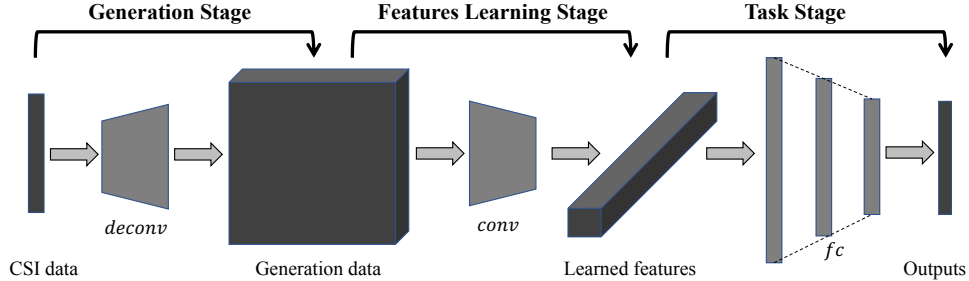


Figure 3: Architecture of CSI-Net. “Generation Stage” transforms CSI sequence to spatially-encoded maps. “Features Learning Stage” extracts features from spatially-encoded maps. “Task Stage” map features to the output of individual tasks. CSI-Net can handle multiple tasks simultaneously by parallelizing multiple task stages after the shared “Generation Stage” and “Features Learning Stage”.

Tool	Protocol	Subcarrier number
Linux 802.11n CSI Tool[50]	802.11n	30
USRP+GNU Radio[51]	802.11g	52(data)+4(pilots)
Atheros CSI Tool[52]	802.11n	56(20MHz), 114(40MHz)

Table 3: Three software tools that produces CSI of multiple subcarriers. The number of subcarriers corresponds to the *channel* number of the input tensor of CSI-Net.

to visual information of the same natural world at three different frequency sets. Similarly, WiFi signals sense the same natural world at N_{sc} electromagnetic frequencies (*i.e.*, N_{sc} subcarriers). Moreover, from the successful multi-channel signal models, such as blind signal separation (BSS) [53], the combined signals can be well-approximated as a linear combination among channels. We keep the interaction among channels while release the information within individual channels using convolution computation. Specifically, we take the 30-dimensional CSI sample at each time-stamp as a multi-channel tensor, where each channel is a 1×1 matrix and corresponds to one subcarrier. Finally, the input tensor of CSI-Net for our tasks is $\mathcal{R}^{30 \times 1 \times 1}$.

4.2 Generation Stage

Recent DNN architectures in computer vision community are very powerful and efficient in processing spatial information encoded within image channels. However, there are rare case studies that directly apply DNNs to the $\mathcal{R}^{30 \times 1 \times 1}$ input tensors.

Using transposed convolution (TC), also called deconvolution, we build a generation stage of CSI-Net. The generation stage explore the within-channel for spatial information CSI-Net input tensors while make it possible to take advantages of modern DNN architectures on images. TC is widely used in Generative Adversarial Nets (GANs) to for image generation [54, 55]. Specifically, We here stack 8 transposed convolution layers (7/8: kernel size of 4×4 , 1/8: kernel size of 3×3) to process the $30 \times 1 \times 1$ input tensor, and produce a tensor of $6 \times 224 \times 224$. The target tensor size is set to 224×224 is because it is a common input size of CNN architectures excluding VGG-nets [22], Inception[23] and ResNets[24], hence easier in tuning hyperparameters. We prefer the transposed convolution with size of 4×4 for there exist abundant successful applications in [56, 57, 58]. All 4×4 kernels are to double the size of feature maps, while one 3×3 kernel is to upsample the size from 4×4 to 7×7 , so the output height/width sizes of every layer are 2, 4, 7, 14, 28, 56, 112 and 224, respectively. Please see Table 15 for more details of generation stage processing on input tensor at every layer.

4.3 Features Learning Stage

Feature learning stage takes the $6 \times 224 \times 224$ tensor from the generation stage and extracts features for final tasks. Following the fashion in computer vision, we call the networks in feature learning stage as the backbone network. Given image-like tensors after the generation stage, various modern CNN architectures, such as AlexNet [21], VGG-nets[22], Inception clusters[23, 59, 60, 61], ResNets[24], and DenseNet [25] can be potentially used as backbone with slight revisions. Following the insights in [62], we select ResNet for it is generally more powerful than AlexNet, has less parameters than VGG-nets, Inception Net and DenseNet. For our current experiment, we prefer not to use heavy networks because we have relatively small dataset (40K CSI samples) comparing to benchmark computer vision

databases (COCO dataset with 330K images). Heavy networks are prone to overfit. The results of 9 networks, including ResNet-18, ResNet-152, Inception-V4, VGG-19 *etc.*, are listed in the ablation experiments, Section 6.6. More results on backbone networks will be shown there. ResNet-18 produced the best performance in these experiments.

4.4 Task Stage

The task stage is to leverage features learned above to compute the outputs for a specific task. It is composed of several fully-connected layers, activation function and loss function.

Fully-connected layers re-weight the features to produce an output vector for a task. As shown in Table 4, to estimate 4 biometrics, *i.e.*, human body fat rate, muscle rate, water rate and bone rate, the output dimension is 4. Human identification is conducted among 30 subjects, so the output dimension is 30. Because the fully-connected layer has much more parameters than convolution layers, which increases the complexity of CSI-Net and difficulty in optimization, we tend to use more convolution layers than fully-connected layers. In our experiments, we only use one fully-connected layer.

Activation function and loss function are used to compute the loss in training CSI-Net, which measures the difference between the network outputs and the ground-truth values. In the biometrics estimation task, we use Rectified Linear Unit (ReLU)[63] plus L1 to compute loss. In other tasks, the SoftMax activation and Cross Entropy function are combined to generate loss.

Data Sizes / Tasks	Biometrics Estimation	Human Identification	Sign Recognition	Falling Detection
CSI-Net Input	$30 \times 1 \times 1$	$30 \times 1 \times 1$	$30 \times 1 \times 1$	$30 \times 1 \times 1$
Generation Stage	$6 \times 224 \times 224$	$6 \times 224 \times 224$	$6 \times 224 \times 224$	$6 \times 224 \times 224$
Feature Learning Stage	256	256	128	128
Task Stage	4	30	10	2
CSI-Net Output	4	30	10	2

Table 4: Tensor sizes at different stages of CSI-Net. Four sensing tasks have the same input size $channel \times height \times width$: $30 \times 1 \times 1$. After generation stage, the spatially-encoded maps are of size $6 \times 224 \times 224$. The outputs of feature learning stage were set differently for the best performance of each task. The output sizes at the task stages are task-specific: Output size 4 for four scalars in biometrics estimation; Output size 30 for 30 subjects used in human identification; Output size 10 for hand signs encoded by 0 to 9; Output size 2 for falling is detected or not detected. The final output size of CSI-Net is the same as output size of task stages.

4.5 Configuration on Different Tasks

For different sensing tasks, the output functions and intermediate tensors are different, as illustrated in Table 4. Taking the task of biometrics estimation as an example, the input tensor size is $Channel \times Height \times Width$: $30 \times 1 \times 1$. After the generation stage, the tensor is $6 \times 224 \times 224$. Then, 256 features are extracted by the feature learning stage. At last, the task stage estimate four biometrics (4 scalars) from the 256 features. The output tensor size of CSI-Net is equal to the output size of task stage. More implementation details of CSI-Net on different sensing tasks are presented in Section 5.

5 Implementation Details

In this section, we present the implementation details of CSI-Net, including the preparing dataset and training CSI-Net.

5.1 Preparing Datasets

The dataset preparation consists of testbed setup, CSI collection, filter design, training/test data split and data augmentation.

5.1.1 Testbed setup

We employed Commodity Off-The-Shelf (COTS) devices to setup our testbed. We replaced the network interface card (NIC) with Intel 5300 NIC at 2 mini-PCs (32G SSD, 1G memory, Ubuntu 14.04 OS). One mini-PC worked as the WiFi signal transmitter (Tx), while the other worked as the receiver (Rx). Both of them were installed with Linux 802.11n

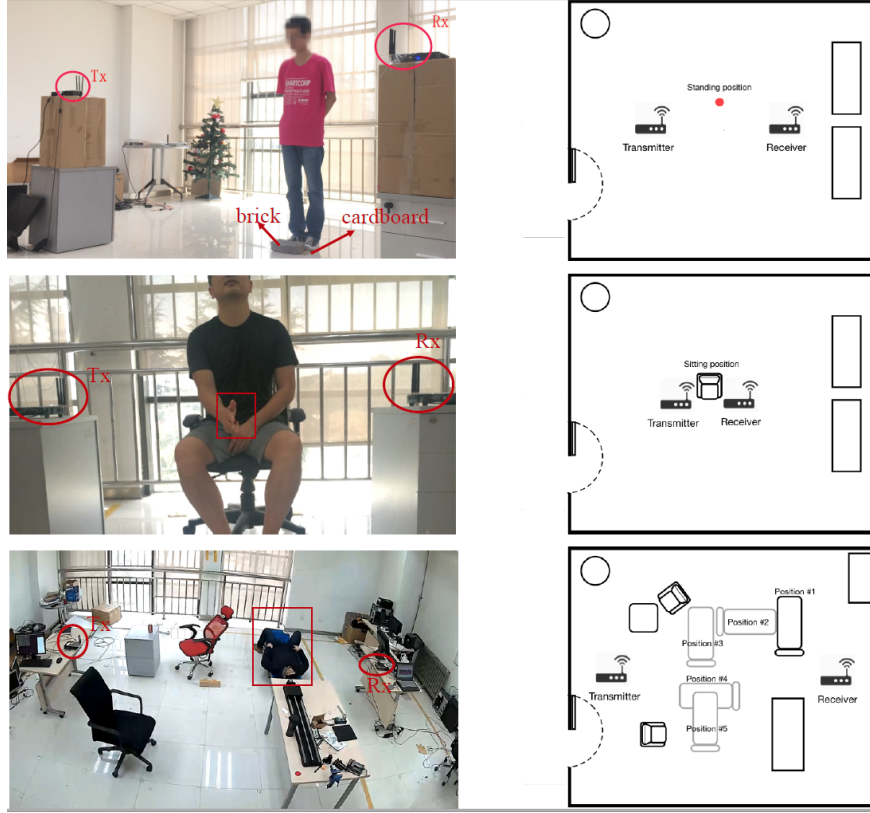


Figure 4: Data collection site snapshot and room layout. Figures from top to down are for biometrics estimation/human identification, hand sign recognition and falling detection. In biometrics estimation, a pasted cardboard and a brick are used to limit the position and orientation of subjects. Setting in sign recognition is an imitation of [2]. In falling detection, we collected data from 5 selected positions, shown in gray at the lower right layout figure.

CSI Tool[50] for parsing CSI. The Tx and Rx were deployed in a room (about $5m \times 6m$) with ordinary furnitures such as tables, chairs and desks. More setup details are listed in Table 5.

5.1.2 CSI data collection

CSI samples were recorded when subjects keep stationary poses or gestures during data collection. The CSI sampling rate was set to 100Hz for all tasks below.

1. **Biometrics Estimation:** we recruited 30 subjects, measured some biometrics of their bodies with Mi® body composition scale[49], and listed the information in the Table 6. We selectively estimated the body fat rate and body muscle rate because these two metrics indicates what the body shape a person has. We also estimated the water rate and bone rate, which are essentially related to the human body internal composition.

As shown in Fig. 4, subjects were asked to stand at a predefined position. To avoid potential CSI biases caused by human position and orientation, we marked the standing position with a brick putting on the pasted cardboard, as shown in Fig. 4. To avoid impacts from the presence of other persons in the environment, we first turned on the CSI tool in the Tx and Rx to record CSI series, while keeping the room without any person. Then a subject walked to the marked position and kept stationary pose. 100-second CSI series, or about 10k samples (at 100Hz), were collected for each subject. We performed this procedure for 30 subjects and generated around 300k CSI samples for the biometrics estimation task. During the dataset collection, we did not change controllable environment settings, such as the height of Tx and Rx, distance between Tx and Rx, placement of furnitures, *etc.*

2. **Human Identification:** we reused the sampled CSI for biometrics estimation to identify human. Actually, we trained a CSI-Net with 2 separate task stages, one for biometrics estimation and another for human identification, with the same inputs.

System Settings/ Tasks	Biometrics Estimation	Human Identification	Sign Recognition	Falling Detection
Tx-Rx Height	1.2m	1.2m	0.8m	0.8m
Tx-Rx Distance	1.6m	1.6m	0.6m	3.0m
# of Subjects	30	30	1	1
Subject Body Pose	standing	standing	siting	standing&laying
# of Positions	1	1	1	5
Sampling Duration	100s	100s	60s	30s
Sampling Rate	100Hz	100Hz	100Hz	100Hz
CSI Samples	300K	300K	60K	30K
Center Frequency	5GHz	5GHz	5GHz	5GHz

Table 5: System settings in experiments. Taking biometrics estimation for example, the transmitter (“Tx”) and receiver (“Rx”) are put on two boxes with height of 1.2m from the floor (“Tx-Rx Height”) and distance (“Tx-Rx Distance”) of 1.6m . We asked 30 subjects to be “standing” in the room. The CSI data were recorded for 100 seconds with sampling rate of 100Hz. The total number of CSI samples is 300k ($30 \times 100 \times 100$). The transmitter and receiver were set to work at 5GHz WiFi band.

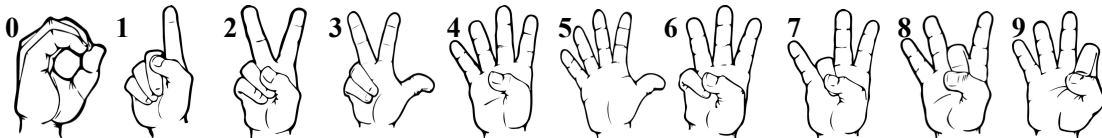


Figure 5: American sign language from 0 to 9 [65].

3. Sign Recognition: for a proper comparison with non-adapted DNNs work, we imitated the experiment setting shown in a prior work [2] to collect CSI dataset for hand sign recognition. The imitations include the same selection of hand signs, height of Tx and Rx, and distance between Tx and Rx, even similarly asking subjects to sit on a chair *etc.* In particular, in our experiment one subject was asked to sit on a chair to pose 10 signs sketched at Fig. 5 (one for 60 seconds). We reduced the height of Tx-Rx(0.8m) to fit the height of the subject’s hand when sitting. Meanwhile, we decreased the distance (0.6m) between Tx and Rx to enhance the sensitivity of CSI variance on different postures, such that micro and similar hand signs can be distinguished. We also kept the controllable surrounding environment unchanged with the same requirement depicted in the biometrics estimation part.
4. Falling Detection: we selected 5 positions in the room and asked one subject to act action of standing and laying (the duration of each action is about 30 seconds), where the laying was to simulate the human body state of fallen down. To protect the subject, we prepared a camp bed for laying. After recording the CSI in one position, the camp bed was moved to next position and the CSI series were recorded again. In this experiment, We enlarged the distance between Tx and Rx to 3.0m for examining the effectiveness of detecting the falling activity in a larger area. Finally, the CSI samples recorded at all positions when the subject is laying were labeled as a category of falling down, while the samples recorded when the subject is standing at the corresponding positions were annotated as not-falling down. Still, we kept the controllable surrounding environment unchanged with the same requirement shown in the biometrics estimation part. The corresponding site figure and layout figure are shown in Fig. 4 (bottom).

5.1.3 Filter design

The raw CSI sequences contain considerable noise. An example is shown in the top subfigure in Fig. 6, where the raw CSI is the data of the 15th subcarrier of the 5th subject in the human identification experiment.

To remove noise in the raw CSI sequences, researchers applied digital filters [1, 7, 32], discrete wavelet transform (DWT)[11, 12, 13], and their combinations[14, 3, 15]. Following the above techniques, we sequentially employ two time domain filters, *i.e.*, the median filter and mean filter, and one frequency domain filter, *i.e.*, the Butterworth filter.

1. Median Filter: In the uppermost subfigure of Fig. 6, there exist too many extremely high/low values (outliers) in the raw CSI. To remove these extreme values, we apply a median filter with sliding window size of 20 and stride of 1. The results are drawn in the 2nd subfigure, which shows a notable performance of the median filter in removing extreme values.

No.	Sex	Fat Rate (%)	Muscle Rate (%)	Water Rate (%)	Bone Rate (%)	Height (inches)	Weight (lbs)
1	Male	5.0	89.7	65.1	13.0	70.5	113.8
2	Male	5.0	89.9	65.1	13.0	66.1	107.9
3	Male	14.3	81.2	58.7	4.1	68.1	141.2
4	Male	7.3	87.8	63.5	8.7	68.5	121.0
5	Male	8.4	86.7	62.8	7.5	66.9	118.9
6	Female	22.9	72.8	52.8	2.3	62.6	104.7
7	Male	12.7	82.7	59.8	4.7	70.9	143.7
8	Male	18.9	76.9	55.6	2.9	71.3	161.7
9	Male	9.9	85.3	61.7	6.2	71.3	134.2
10	Male	15.0	80.5	58.2	3.9	65.0	127.9
11	Male	11.0	84.3	61.0	5.5	70.5	138.3
12	Male	18.9	76.8	55.6	2.9	66.9	148.2
13	Female	12.7	82.6	59.8	4.7	62.6	114.5
14	Female	17.5	78.0	56.5	3.2	63.8	105.4
15	Female	16.9	78.2	56.9	3.4	66.5	109.1
16	Female	26.2	69.4	50.6	1.9	63.4	121.9
17	Male	20.9	75.0	54.2	2.6	68.5	161.2
18	Female	17.2	78.3	56.7	3.3	64.2	105.9
19	Female	22.5	73.2	53.1	2.4	63.0	104.8
20	Male	25.1	70.9	51.3	2.0	71.7	190.5
21	Female	24.9	70.9	51.4	2.1	61.8	106.0
22	Female	30.9	65.2	49.2	1.6	60.6	118.4
23	Female	22.0	73.7	53.5	2.4	62.2	102.1
24	Male	10.1	85.2	61.6	6.1	69.3	128.9
25	Female	20.9	74.4	54.2	2.6	62.6	110.6
26	Female	20.8	74.4	54.2	2.6	65.4	110.6
27	Male	20.8	75.0	54.2	2.6	68.9	162.5
28	Male	14.4	81.1	58.6	4.1	66.9	135.4
29	Male	23.5	72.5	52.4	2.2	72.8	187.9
30	Male	22.3	73.6	53.2	2.4	65.0	152.7

Table 6: The information of 30 recruited subjects. All biometrics were measured using a body composition scale which embedded the module of Bioelectrical Impedance Analysis(BIA)[64]. Subjects were asked to stand on the scale after removing shoes and socks. All metrics were recorded when the reading of scale is stable.

2. Mean Filter: We then utilize a mean filter (sliding window size of 20, stride of 1) to remove slight oscillations in the CSI sequences that filtered by the median filter. The results are shown in the 3rd subfigure of Fig. 6, where the oscillations in CSI are defeated well.
3. Butterworth Filter: At last, a low-pass Butterworth filter (5th order, passband of 5Hz) is applied to remove high-frequency noise for pursuing a much smoother CSI sequences. We show the results in the 4th subfigure of Fig. 6.

5.1.4 Training/Testing sets.

Note that CSI sequences drift along time Fig. 6 due to several factors: First, the Intel 5300 NIC is imperfect and severely suffers from noises. The impacts include uncertainty in the packet boundary detection and mismatch in sampling frequency [52]. Second, human heartbeat and respiration may introduce periodic noises [6, 7]. The last but not the least, it is very hard for subjects to keep completely stationary for more than 100 seconds (CSI collecting duration of biometric estimation and human identification task), although they have been asked to keep stationary. Randomly splitting training and testing is equivalent to use all data for training and testing.

As illustrated in the last subfigure of Fig. 6, in all tasks, we used the first 4/5 CSI sequences for training and the remaining 1/5 for testing. We took this splitting strategy to simulate the practical scenarios, where one first collects data and trains a network, then tests incoming data.

To make CSI-Net more robust to CSI noise, before to train CSI-Net, we further perform two operations on CSI sequences:

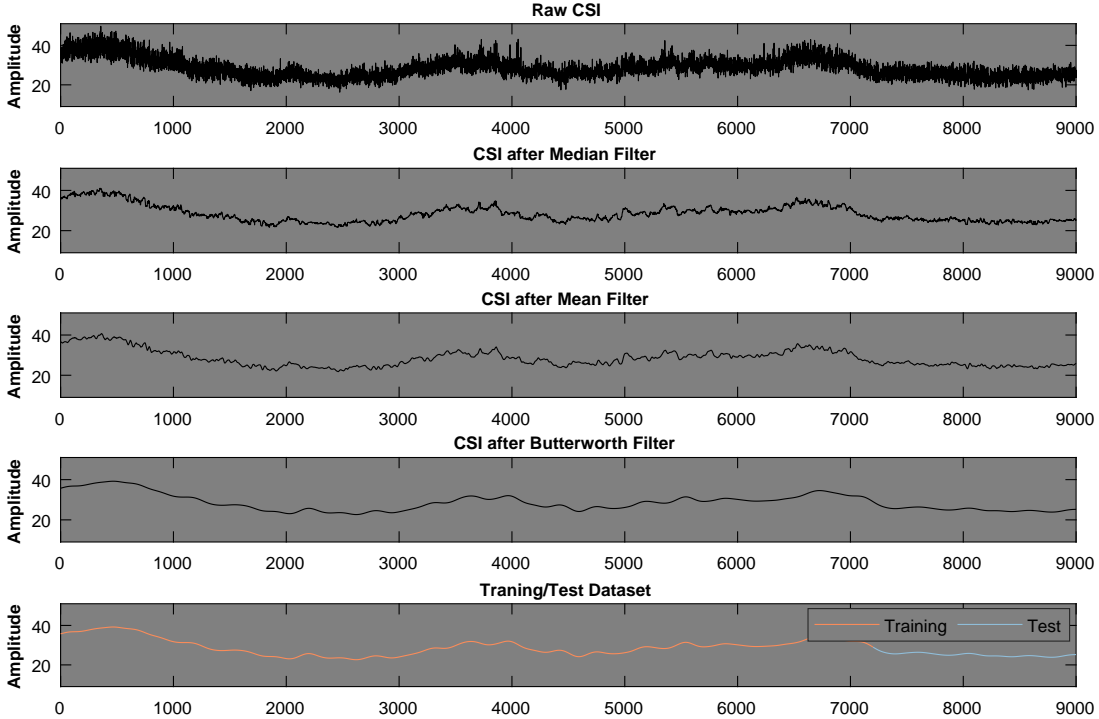


Figure 6: Noise filtering and splitting of Training/Test sets. Example: a CSI sequence of the 15th subcarrier recorded for the 5th subject in the human identification experiment. The first three sub-figures shows that, given the noisy raw CSI sequence, we used a median filter to remove extremely high/low values, a mean filter to smoothen the sequence, and a low-pass Butterworth filter to remove high-frequency noise and further smoothen the sequences. The last subfigure illustrates that, for CSI sequences of one subject, the Training/Test sets were split as follows: 4/5 CSI sequences were used for training, while the remaining 1/5 CSI sequences were used for test.

- **Local Temporal Average:** To smooth temporal random noise, we compute the average of every 10 continuous CSI samples with stride of 10, and use the average value as one input sample for CSI-Net.
- **Augmenting Training Data:** Due to the drift of CSI sequences. CSI-Net would perform well in training data but fail on test data, which is known as the overfitting problem. We propose a data augmentation method to address this problem (see Algorithm 1 for this problem). The main idea is to deliberately introduce some jitter CSI to the training data, so that CSI-Net can learn to model more data variances.

Specifically, denote the original training set as S , in which samples are from s_1 to s_n . The data augmentation algorithm runs in multiple iterations. In a certain iteration, for example the iteration of $k = 2$, the instances in S are randomly shuffled. Then, we compute the averages of every 2 adjacent instances with stride of 2, and input them as new instances into augmented dataset S' . We iteratively perform this operation 4 times ($k = 2, 3, 5, 7$). At last, combing the augmented items with the original training set generates the augmentation set to train networks. The key operation of this algorithm is averaging the shuffled training instances, which makes CSI-Net to be trained with much more CSI patterns. Thus, it would be more resilient to the unpredictable CSI in the test phase. In our experiments, this augmentation approach significantly increased the human identification accuracy from 78.26% to 93.00%.

We applied above two operations for the dataset of all tasks. In Table 7, the numbers of training samples for biometrics estimation, human identification, hand sign recognition and falling detection are 38,633, 38,633, 21,428 and 21,879, respectively. These numbers are sufficiently big for training our deep neural network, *i.e.*, CSI-Net. The numbers of test instances for 4 tasks are also listed in Table 7.

5.2 Training Networks

CSI-Net was implemented in *Pytorch* 0.4.1 and trained on a Ubuntu server with 4 Titan Xp GPUs. The optimizer is Adam[66] with default parameters ($\beta_1 = 0.9, \beta_2 = 0.999$). We train the networks for 20 epochs with a minibatch size

ALGORITHM 1: Data Augmentation

Input: Original Training Set: $S = \{s_1, s_2, \dots, s_n\}$ **Output:** Augmented Training Set: S' Initialize $S' = \{\}$ **for** $k \in [2, 3, 5, 7]$ **do** Shuffle $S \rightarrow S^* = \{s_1^*, s_2^*, \dots, s_n^*\}$ Initialize $S_k = \{\}$ **for** $i \in [1, 2, \dots, \lfloor n/k \rfloor]$ **do** Average k continuous shuffled instances $\frac{1}{k} \sum_{(i-1)k+1}^{ik} s_i^* \rightarrow s'_i$ $s'_i \cup S_k \rightarrow S_k$ **end** $S_k \cup S' \rightarrow S'$ **end** $S' \cup S \rightarrow S'$

Sets /Tasks	Biometrics Estimation	Human Identification	Sign Recognition	Falling Detection
#Training instances	38,633	38,633	21,428	21,879
#Test instances	4,444	4,444	2,468	2,519

Table 7: The training/test “Sets” for four sensing tasks. For example, the tasks of biometrics estimation and human identification used 38, 633 training instances and 4, 444 test instances, respectively.

of 20 and initial learning rate of 0.001. The learning rate is decayed by 10% at the epoch of $\{4, 7, 10, 13, 16, 18\}$. In the beginning of each epoch, the training data is shuffled.

5.2.1 Network Architecture

1. **Biometrics Estimation and Human Identification:** Having mentioned in the data preparation section, we use the same dataset for biometrics estimation and human identification. Thus, we design one network with two separate task stages to jointly achieve the both. This network is composed of **shared layers** and **task-specific branches**. In Section 9.3, we sketch the network in Fig. 13, list the parameters of shared layers in Table 15, and exhibit the parameters of biometrics estimation branch and human identification branch in Table 16 and Table 17, respectively. In the shared layers, 8 transposed convolution layers are to generate spatially-encoded maps with size of $6 \times 224 \times 224$ (6 channels, height/width of 224). Besides, 17 convolution layers (on the basis of ResNet-18[24]) are to generate shared feature maps with size of $512 \times 7 \times 7$. In the branch for biometrics estimation, the shared feature maps are converted to 4 values for estimating 4 target biometrics (body fat/muscle/water/bone rate) by 2 convolution layers and 1 fully-connected layer. Similar to this, in the branch for human identification, the shared feature maps are converted to 30 values for identifying these 30 involved subjects. Meanwhile, Batch normalization [59] and ReLU [63] activation follow every transposed convolution layer and convolution layer.
2. **Sign Recognition:** We fully reuse the DNNs architecture of biometrics estimation and human identification by replacing their task-specific branches with branch for hand sign recognition. The branch for hand sign recognition is also composed of 2 convolution layers and 1 fully-connected layer, where two subtle differences exist comparing to those for biometrics estimation and human identification. First, the output size is 10 for recognizing 10 hand signs. Second, the number of channels is reduced to 128 because we consider this task has lower complexity than jointly identifying human and estimating biometrics and hence requires less parameters to fit. More details are shown in Fig. 13 and Table 18 in Appendix.
3. **Falling Detection:** We still reuse the DNNs architecture for biometrics estimation and human identification to solve falling detection task by replacing task-specific branches with branch designed for falling detection. The specific branch is also composed of 2 convolution layers and 1 fully-connected layer. The output size is 2 for 2 classes: fallen or not fallen. More details are shown in Fig. 13 and Table 19 in Appendix.

5.2.2 Loss Function

- **Biometrics Estimation and Human Identification:** We set the *loss* of the jointly-trained tasks, denoted with L , as follows,

$$L = L_{bio} + \alpha L_{id} \quad (5)$$

where L_{bio} and L_{id} are the *losses* of biometrics estimation and human identification, respectively. α works as a importance balance between both tasks. L_{bio} is the sum of 4 biometrics estimation *losses* that are computed by L1 Loss, and the L_{id} is computed by the Cross Entropy Loss. Following settings in Fast R-CNN[18], we normalize the biometrics values within [0,1] before training, meanwhile, we set the balance α to 1, which means we equally treat the importance of both tasks.

- Sign Recognition: We compute the *loss* of hand sign recognition by

$$L = -\log p_i \tag{6}$$

where p_i is the i -th SoftMax result of an instance that is with a true label of i . Actually, this is one of writing styles of the Cross Entropy Loss.

- Falling Detection: The Cross Entropy Loss is also applied to compute the *loss* of falling detection task.

6 Result and Discovery

In this section, we first present accuracies of CSI-Net on 3 classification tasks, *i.e.*, human identification, sign recognition and falling detection, and make a comparison with prior work. Then we depict CSI-Net performance on all 4 tasks detailedly. Besides, We show some discoveries about behaviors of CSI-Net processing CSI data. We also list the performance of 9 different backbone networks, including ResNet-152, Inception-V4 and VGG-19. We find that ResNet-18 performed best for our datasets. In addition, we modify the generation stage and propose a new version of CSI-Net. The new CSI-Net is lighter but works better, we call it CSI-Net V1.5.

6.1 Accuracy Comparison

We show accuracies of CSI-Net on 3 classification tasks, *i.e.*, human identification, hand sign recognition and falling detection, in Table 8. Meanwhile, accuracies achieved by Support Vector Machine (SVM) and Naïve Bayes, are listed as the baseline. For SVM, we use LibSVM[67] with radial basis function kernel ($\gamma = 1/30$), L2 regularization and penalty of 1. Naïve Bayes is implemented with assumption that CSI data follows Gaussian distribution. Features used in SVM and Naïve Bayes are the CSI amplitudes of 30 subcarriers, similar to the CSI-Net. The only difference is that the input size of CSI-Net is $30 \times 1 \times 1$, but the input size of SVM and Naïve Bayes is 30×1 . Due to limited space, we leave more technical details about SVM and Naïve Bayes in the Appendix, Section 9.1 and Section 9.2. As aforementioned in Section 5.1.2, we collected CSI under controllable environment and kept CSI parameters unchanged, such as the Tx/Rx settings, orientations and position of subjects. CSI-Net is able to learn the differences in human body or human pose, not the changes in the environment when collecting data.

Method	Accuracy		
	Human Identification	Sign Recognition	Falling Detection
CSI-Net	93.00%	100%	96.67%
SVM-RBF	85.28%	90.24%	81.46%
Naïve Bayes	72.97%	81.00%	73.01%
Prior work	79.28%-50[26], 80%-6[27],91%-11[17]	90.2%[2], 93%[14]	90%[33], 91.5% [5],93%[11]

Table 8: Classification accuracy comparison. “SVM-RBF” stands for the C-SVC with radial basis kernel implemented in LibSVM [67]. “Naïve Bayes” was implemented with assumption that CSI data follows Gaussian distribution. Existing work on human identification were conducted on different number of subjects, denoted as $xx\% - \#subjects$.

From Table 8, we see accuracies of CSI-Net on three classification tasks are 93.00%, 100% and 96.67%, respectively. Apparently, CSI-Net outperforms SVM and Naïve Bayes in all three tasks. The results imply that CSI-Net is able to automatically learn and establish better representation for human sensing than SVM and Naïve Bayes. The results also verify our assumption that CSI variance caused by static postures can be used for human sensing.

A comparison with closely-related prior work is also shown in Table 8. Here we only focus on comparing data processing methods and illustrate that CSI-Net is an alternative method to do different tasks. The systems in Table 8 are built to detect human activities in motion but CSI-Net is to detect human stationary poses. Besides, the accuracy of those work are evaluated in diverse scenarios, such as in different rooms. To apply CSI-Net to a new environment, further data collection and training are needed. Other these differences, we have tried our best to imitate these work with the same settings in data collection, please see Section 5.1.2 for more details in data collection. Taking human identification as an example, the approach in [26] tested on 50 subjects with identification accuracy of 79.28%, the work in [27] tested on 6 subjects with accuracy of 80%, and the method in [17] got significantly better accuracy, *i.e.*,

91% with activities like opening microwave oven, while only testing 11 subjects. CSI-Net outperforms them in the comprehensive aspect of identification accuracy and number of test subjects (30 subjects). Besides, CSI-Net is able to jointly estimate human biometrics with identification. CSI-Net also achieves a higher accuracy in sign recognition and falling detection compared to prior methods. The notable performance demonstrates the distinguished generic ability of CSI-Net for human sensing tasks including body characterization and activity recognition.

6.2 Biometrics Estimation

To evaluate the results of biometrics estimation, we apply two metrics, *i.e.*, mean average error (*mAE*) and mean square deviation (*mSD*). The former is to measure the estimation error of CSI-Net, and the latter for the estimation variance. The *mAE* is computed as follows.

$$e_k = \frac{1}{N_k} \sum_{i=1}^{N_k} |s_{k,i}^* - s_{k,i}| \quad (7)$$

where the e_k represents the average estimation error of the k -th subject, $s_{k,i}$ stands for the real i -th test value of the k -th subject, $s_{k,i}^*$ represents the estimation value, and N_k is the volume of test data of the k -th subject. The metric, *mAE*, is the *mean* of all average estimation errors ($e_k, k \in [1, 30]$).

$$mAE = \frac{1}{30} \sum_{k=1}^{30} e_k \quad (8)$$

mSD is computed in a similar way.

	Fat Rate	Muscle Rate	Water Rate	Bone Rate
<i>mAE</i>	1.11	1.00	0.71	0.38
<i>mSD</i>	0.58	0.50	0.24	0.07
min-max range	[5.0, 30.9]	[65.2, 89.9]	[49.2, 65.1]	[1.6, 13]

Table 9: The mean Average Error (*mAE*) and mean Square Deviation (*mSD*) of four biometrics estimation tasks. Note that comparing to the numerical range of biometrics, CSI-Net produced very small *mAEs* and *mSDs*. To our knowledge, no existing work estimates these biometrics using WiFi signals.

As shown in Table 9, CSI-Net achieves very small *mAEs* and *mSDs* comparing to the numerical range of 30 subjects' biometrics. Taking the fat rate estimation result as an example, the average estimation error is 1.11, which can be considered as a small error because the min-max range of fat rate is [5.0, 30.9], as listed in Table 6. Besides, the estimating variance is 0.58, indicating that CSI-Net has an excellent performance in terms of stability. The results demonstrate that human body does incur strong CSI variance which can be effectively utilized to estimate the human biometrics.

In Fig. 7, we draw a set of radar charts to visualize the estimated biometrics of 30 subjects. In each chart, the four axes (right/up/left/down) correspond to four human biometrics (fat/muscle/water/bone rate). In the figure, the red lines stand for the average estimation values. The green lines represent the ground truth of biometrics measured by the Mi® body composition scale[49]. The majority of blue lines are perfectly overlapped with the red lines, implying that CSI-Net can estimate biometrics accurately for every subject.

More importantly, Fig. 7 shows that CSI can potentially be used to assess body state information for health care. For example, the results accurately estimate that some subjects (1st, 2nd, 4th, 5th, 9th, 13th and 24th) are with low fat rate and high muscle rate. On the other hand, some subjects (6th, 16th, 22th and 29th) are with high fat rate and low muscle rate. Accordingly, we can give them useful suggestions, *e.g.*, enriching the diet or doing more exercises. Using CSI-Net, we can also detect some potential threats to human health. For example, some subjects (3th, 19th and 21th) are with low bone rate, indicating that they should increase the intake of *calcium-rich* foods, such as shrimp, bean and milk. This makes it possible to build daily health maintenance application wherever there is WiFi.

6.3 Human Identification

We evaluate human identification results with the confusion matrix in Fig. 8. The column label is the real human ID and the row label is the predicted human ID. The gray level of block (i, j) represents the ratio that the j -th subject is identified as the i -th subject by CSI-Net. Thus, the value of each block ranges from 0% to 100%. The completely white stands for ratio of 0% and the completely black stands for ratio of 100%. From the figure, we observe that CSI-Net achieves 100% accuracy on most of subjects. There are few errors when identifying the subject of {9, 14, 25, 28}.

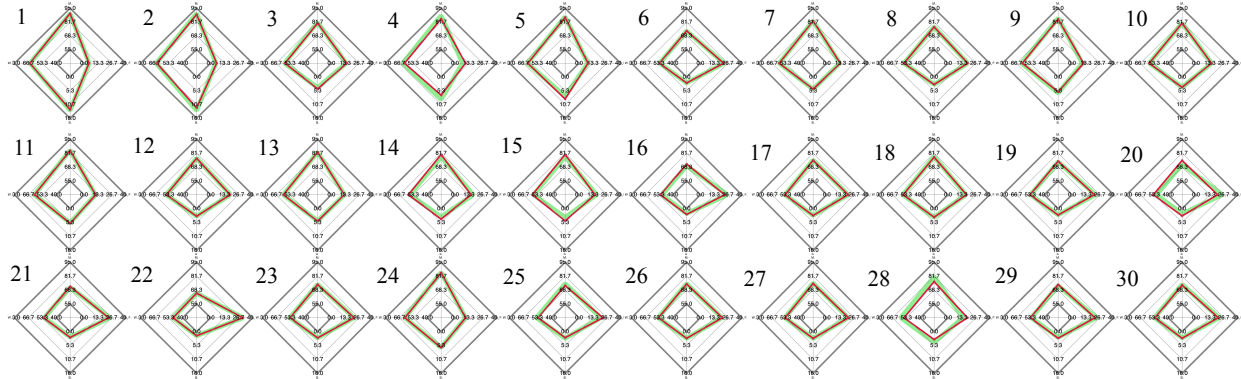


Figure 7: Radar charts of biometrics estimation for 30 subjects. Four axes (right/up/left/down) correspond to four human biometrics (fat/muscle/water/bone rate), the red lines are estimation, the green lines are ground-truth.

Specifically, CSI-Net may incorrectly identify the 8th subject to the 7th subject, 14th subject as the 8th subject, the 25th as the 21th, the 28th as the 15th or 26th.

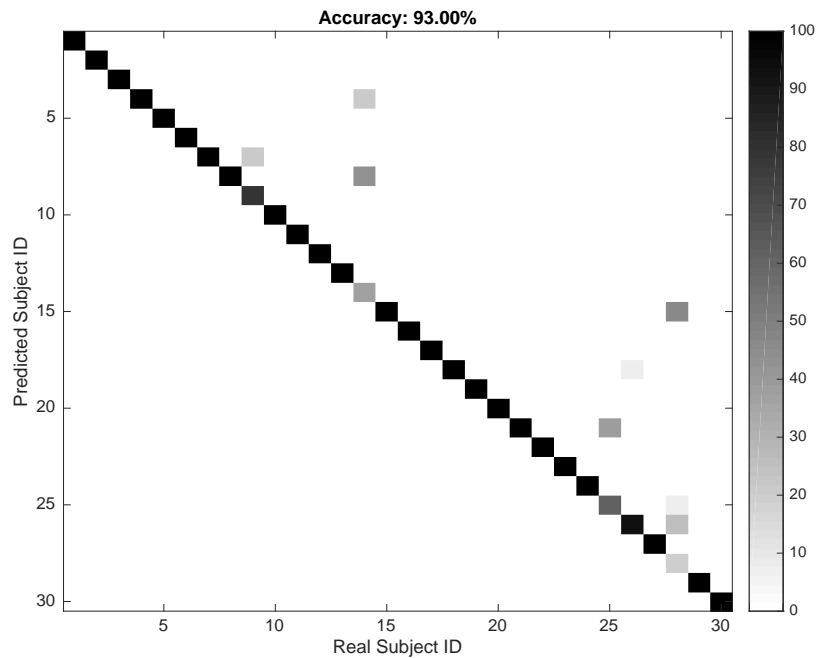


Figure 8: Confusion matrix of human identification for 30 subjects.

To figure out the reason of above mis-identification, we dig the correlation between the human identification and biometric estimation. We defined an indicator, *Error*, as the average of all 4 biometrics estimation errors over 30 subjects. We then used $1/F1, \frac{precision+recall}{2 \times precision \times recall}$, the reciprocal of *F1 score*[68], to exhibit the performance of CSI-Net on human identification. The results are shown as in Fig. 9, where a larger *Error* or $1/F1$ indicates a worse performance of CSI-Net on this subject.

In Fig. 9, we find that CSI-Net is prone to incorrectly identify those subjects who are with high *Error* of biometrics estimation, such as the 14th, 25th, and 28th subjects. While if his/her biometrics are estimated accurately, the identification accuracy of this subject is nearly 100%, such as the subjects of {1, 2, 3, 5, 6, 7, 8, 10, 11, 12, 13, 17, 18, 19, 21, 22, 23, 24, 26, 27, 29, 30}. We further compute the *Pearson Correlation Coefficient*[68], between *Error* and $1/F1$. The result is 0.63, which means, statistically[69, 70], there exists a strong correlation between biometrics estimation and human identification. According to this correlation, we infer that the reason of mis-identification that CSI-Net may learn to identify subjects with features that encoded in their biometrics. We have done further work to shown this inference and depict the work in the coming paragraphs of Section 6.7.

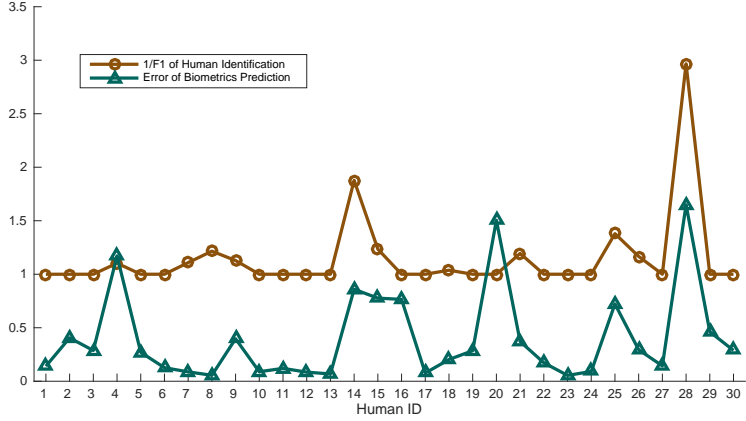


Figure 9: Correlation between the performance of biometrics estimation and human identification.

6.4 Sign Recognition

We also illustrated the results of hand sign recognition with a confusion matrix in Fig. 10. The column label is the real hand sign and the row label is the predicted hand sign. In this figure, we find that using our dataset CSI-Net achieves an accuracy of 100%. This extremely high accuracy demonstrates that micro human postures can result in CSI variances. Meanwhile, even the variances caused by very similar hand sign gestures can be well recognized by CSI-Net. Because with the same features as applied to CSI-net, the accuracy achieved through SVM is 90.24%, which is much worse than that of CSI-Net. It is safe to say that CSI-Net is a better classifier to recognize hand sign with CSI data. Besides the power of CSI-Net, we think another reason of achieving high accuracy is that we deployed the transmitter and receiver with a short in-between distance and asked the subject to pose in the line-of-sight, which made CSI very sensitive to the changes caused by gestures.

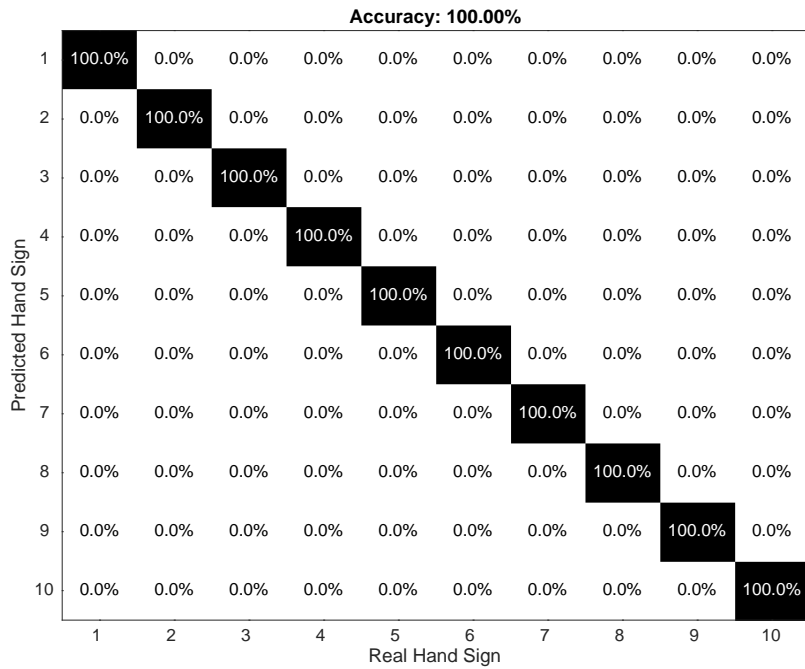


Figure 10: Confusion matrix of sign recognition. CSI-Net predicted sign of {0, 2, 3, 4, 5, 6, 7, 8, 9} with 100% accuracy. Only 5.6% error occur where some “1”s were recognized as “8”.

6.5 Falling Detection

The results of falling detection task are listed in Table 10, where the accuracy of CSI-Net detecting falling is 98.73%. In practice, this is a high detection accuracy. Still, CSI-Net wrongly predicts falling activities to standing case with ratio of 1.27%, and incorrectly thinks standing case as falling activities with ratio of 5.41%. This incorrect detection can be solved with a little longer monitoring duration, which allows the system has more samples to vote for a detection results. Here, we do not tend to go deeper in this system optimization, because it is out of main scope of this paper.

We then explain the reason why it is more difficult for CSI-Net to detect human falling (2-class problem) than to recognize hand sign (10-class problem). We mainly ascribe it to 3 differences in the data collection setting between these two tasks. First, in falling detection task, the Tx/Rx distance was set to be nearly 3m. While in the hand sign detection task, the Tx/Rx distance was set to 0.8m, which made CSI more sensitive to human pose change. Second, in the falling detection, we collected CSI from 5 different positions, which was more complex than that of hand sign detection (the data is only collected in one position). Third, in hand sign recognition, subjects were asked to pose hand in the line-of-sight of Tx/Rx. However, the data for falling detection were mainly collected from the non-line-of-sight paths. It is intuitive that the poses occurring in the line-of-sight may raise more distinguished WiFi variances than that of non-line-of-sight ones.

	Real Falling	Real Standing
Detected Falling	1246 (98.73%)	68 (5.41%)
Detected Standing	16 (1.27%)	1189 (94.59%)

Table 10: Confusion matrix of falling detection. CSI-Net predicted falling and standing with accuracy of 98.73% and 94.59%, respectively. The error occurs where it predicts 1.27% of falling to standing, and predicts 5.41% of standing to falling.

6.6 Ablation Experiments

All above results are obtained with the backbone of ResNet-18 [24]. As explained in Section 4, CSI-Net is a scalable architecture and can be easily combined with other good CNN networks, such as VGG-net [22] and Inception [61]. Next, we report the results achieved by these backbones and show that ResNet-18 produced the best results for our datasets, shown in Table 11. In addition, ResNet-18 is the smallest model, shown in Table 12. We believe that ResNet-18 gives the best balance between model complexity and data complexity.

backbone	Human Identification		Sign Recognition		Falling Detection	
	acc (train)	acc (test)	acc (train)	acc (test)	acc (train)	acc (test)
ResNet-18	100%	93.00%	100%	100%	98.13%	96.67%
ResNet-34	100%	85.10%	98.74%	72.69%	96.02%	94.40%
<i>ResNet-50</i>	99.99%	87.51%	99.99%	100%	95.77%	93.85%
<i>ResNet-101</i>	100%	88.41%	99.96%	99.03%	96.14%	93.33%
ResNet-152	100%	88.61%	100%	100%	94.07%	89.68%
<i>Inception-V3</i>	99.94%	82.63%	100%	100%	97.04%	96.35%
<i>Inception-V4</i>	100%	87.60%	100%	100%	96.11%	93.01%
VGG-16	30.03%	18.70%	80.31%	46.67%	87.63%	83.56%
VGG-19	19.03%	16.00%	75.27%	42.30%	88.83	85.15%

Table 11: Result of different backbones. “acc(train)” and “acc(test)” represent training accuracy and test accuracy, respectively.

6.7 Discovery

6.7.1 Generation or Interpolation:

In the generation stage of CSI-Net, 8 stacked transposed convolution layers convert the CSI data to a tensor with height/width 224×224 , which is approximating to conventional input size of CNNs. This idea of applying stacked transposed convolution layers is derived from DC-GAN [71], a work making 1D tensor to an vivid image. However, considering the computation cost of these layers, we explored simpler but still efficient ways to reshape CSI into image-like tensors for CNNs. Then, we had a better deep architecture for our tasks.

backbone	Human Identification	Sign Recognition	Falling Detection
ResNet-18	88MB	61MB	61MB
<i>ResNet-34</i>	127MB	102MB	102MB
ResNet-50	189MB	176MB	176MB
ResNet-101	798MB	366MB	366MB
ResNet-152	878MB	423MB	423MB
<i>Inception-V3</i>	90MB	90MB	90MB
Inception-V4	164MB	164MB	164MB
VGG-16	975MB	531MB	531MB
VGG-19	995MB	552MB	552MB

Table 12: Saved model size.

The first method is to resize CSI tensor from size of $30 \times 1 \times 1$ to size of $30 \times 224 \times 224$ with *bilinear* interpolation, whose performance is shown in Table 13. Surprisingly, this simple method achieves high accuracy in all tasks, which inspired us to reconsider the function of interpolation operation. We think the strength of interpolation is to reduce the amount of parameters to be optimized, which would reduce the risk of over-fitting. However, the weakness of interpolation is that it cannot introduce any nonlinear mapping ability into CSI-Net. So, we try an intuitive idea: combining the transposed convolution layer and interpolation operation to generate spatially-encoded image-like tensors. Recalling that we have 8 transposed convolution layers in CSI-Net, we replace the 2nd, 4th, 6th, and 8th layers with bilinear interpolations, resulting in a lighter CSI-Net. It outperforms the original CSI-Net with a notable increase in the accuracy. The results are shown in Table 13. We call the new architecture **CSI-Net V1.5**.

Method	Human Identification		Sign Recognition		Falling Detection	
	acc (train)	acc (test)	acc (train)	acc (test)	acc (train)	acc (test)
Transposed Convolution (TC)	100%	93.00%	100%	100%	98.13%	96.67%
Interpolation (I)	100%	91.36%	100%	100%	98.12%	93.45%
CSI-Net V1.5 (TC+I)	100%	94.42%	100%	100%	98.07%	97.73%

Table 13: Three methods to make CSI sample image-like tensor. Interpolation means directly resizing $30 \times 1 \times 1$ CSI tensor to be $30 \times 224 \times 224$ with bilinear interpolation. Transposed Convolution represents original CSI-Net. CSI-Net V1.5 (TC+I) is to replace the 2nd, 4th, 6th and 8th transposed convolution layers with interpolation. It is the best of all.

6.7.2 Jointly or Separately:

To validate our inference, from Fig. 9, that CSI-Net may learn to identify subjects with features that encodes biometrics, we built two networks for these two tasks separately. The architectures of these two networks are the same except different task stages (More details were sketched in Fig. 14 in the Appendix).

The result of the two separately-trained CSI-Nets is listed in the Table 14, where the “error” represents the average estimation error of 4 biometrics over 30 subjects. The result shows that jointly-trained CSI-Net outperforms the separately-trained ones in both tasks. It indicates that features encoding information of both human biometrics and identity (jointly-trained), can facilitate both tasks. We think the reason why jointly training works better than separately training is these two tasks, biometrics estimation and human identification, are highly correlated. When CSI-Net correctly identifies a subject, it will tend to estimate his/her biometrics correctly, and *vice versa*. The jointly training introduce double insurances in optimizing CSI-Net, making CSI-Net converge to a state that works better for both tasks.

What is more important, this discovery suggests a practical strategy in data collection and a practical strategy in networks design. For data collection, we should record more aspects of data, for example, when preparing action dataset, the subjects’ identities and biometrics should also be recorded. For network design, we can build an affiliated branch to jointly train networks for some tasks, for example, a branch of human identification can be considered to applied when doing human activity recognition.

	Biometrics Estimation	Human Identification
Jointly-trained performance	error: 0.80	accuracy: 93.00%
Separately-trained performance	error: 0.87	accuracy: 90.94%

Table 14: Result of jointly/separately-trained CSI-Net for biometrics estimation and human identification

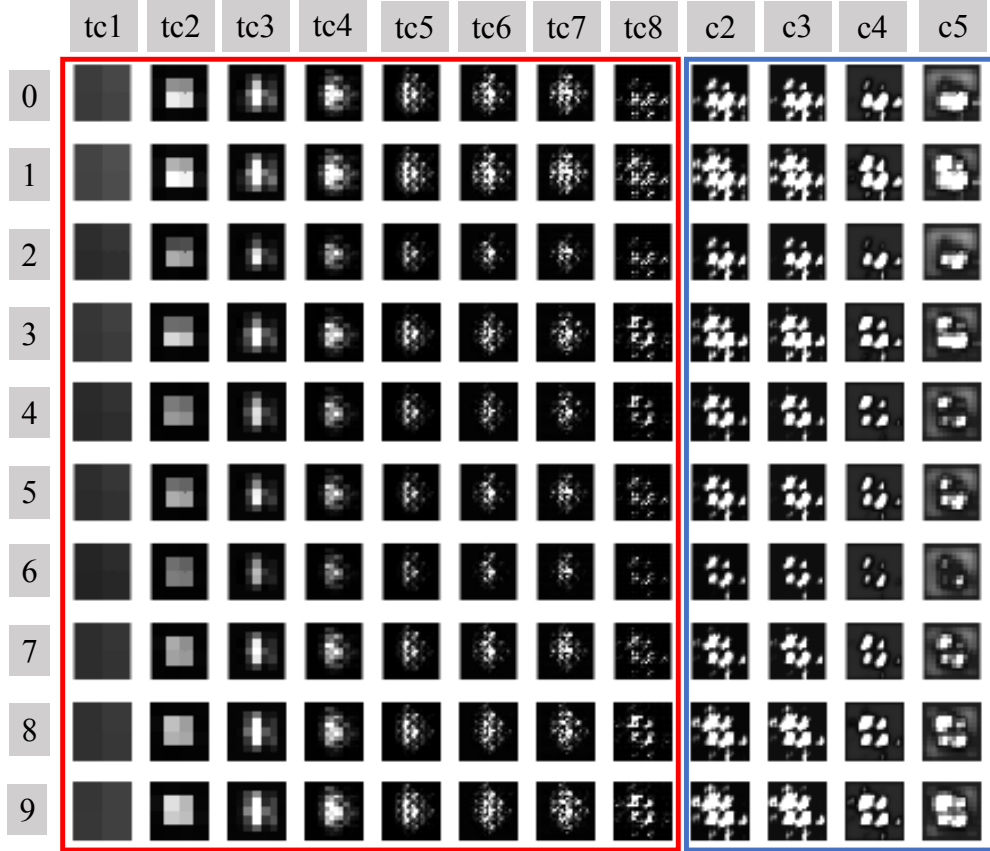


Figure 11: Feature maps of sign recognition to illustrate CSI-Net behavior.

6.7.3 CSI-Net Behavior:

For exhibition convenient, we selectively drew the feature maps of 10 test instances in Fig. 11, correctly-recognized in the task of sign recognition, to illustrate the CSI-Net behavior on processing CSI data. The shown feature maps are the averages along the *channel* and are resized equally. “tc1” is the abbreviation of the “transposedconv_1” in Table 15, similar rule applies to the remaining abbreviations. The output maps of generation stage are in a red box. The output maps of 4 residual blocks[24] are in a blue box. From the figures, we made discoveries listed as follows.

- Feature maps of difference sign categories have little differences after “tc1”, and grow clearly different patterns after “c5”, which means CSI-Net can significantly magnify the distances between different categories.
- Feature maps change sharply after the blocks of “c4” and “c5”, which indicates the powerful representation ability of DNNs appears if we contentiously increase the network depth.
- Feature maps after “c2”, “c3”, “c4” all have four clustered highlights, which implies convolution blocks may dig the details of the feature maps while keeping their spatial framework unchanged.
- The patterns of features maps change after every “tc” layers, which implies that the transposed convolution layers are continuously converting the original CSI (information encoded in subcarriers) to the features (information encoded in the spatial maps).

6.7.4 Spatially-encoded Maps:

We call the feature maps after the generation stage as the **spatially-encoded maps**, in which the original CSI data (information encoded in subcarriers) are transformed to the images (information encoded in the spatial maps). To illustrate this transformation, some correctly-predicted test instances in task of human identification, hand sign recognition and falling detection are drawn in the Fig. 12. We also list our discoveries as follows.

- Information of CSI data is encoded in chess-board-like image.

- The size of highlight points increases when number of categories decreases.

If looking the spatially-encoded maps from the perspective of image resolution, we can regard those maps with larger highlight points having lower resolution because their points are blur and partly-overlapped with each other. Following this assumption, CSI-Net generates high resolution images for human identification, low resolution images for falling detection and median resolution images for falling detection and median resolution images for hand sign recognition. This indicates that CSI-Net can automatically promote the resolution of spatially-encoded maps if the task complexity increase. This may be an essential reason why CSI-Net can handle different tasks including but not limit to what we have tested.

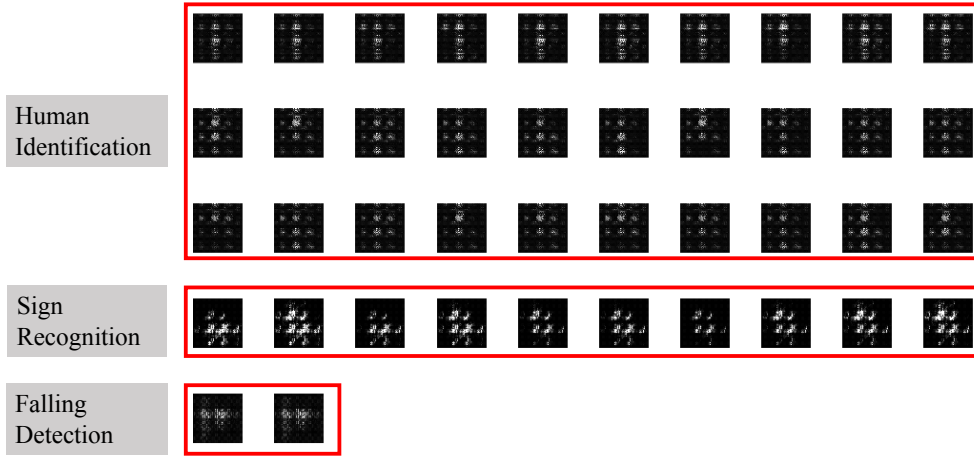


Figure 12: Spatially-encoded maps of human identification, sign recognition and falling detection.

7 Limitation and Future Work

For the task of activity recognition, current version of CSI-Net requires subjects to act the predefined postures then makes prediction among these postures. This requirement is acceptable for activity-specific systems such as those detect the elderly falling. However, there still exist situations that require human motion to be recognized continuously like the surveillance system. Our future work focuses on addressing this limitation.

Recalling that current CSI-Net generates spatially-encoded maps and process CSI data as images. To perform continuous human motion recognition, CSI-Net should **learn spatiotemporal-encoded maps** from CSI sequences. In this way, CSI sequences can be treated as videos. Consulting techniques in computer vision for videos, we are considering two methods to extend CSI-Net for continuous human motion recognition.

1. **Spatio-temporal Convolution Operation:** Three-Dimensional Convolution (C3D)[72], Convolution-Deconvolution-Convolution (CDC)[73] and Temporal Preservation Convolution (TPC)[74] were proposed to conduct action recognition from videos. Those approaches not only extract semantic information (spatially-encoded) of individual video frames but also learn temporal information from continuous video clips. Their experimental results outperform some work built on RNNs like LSTM[75, 76]. CSI-Net is based on single-image convolution, so it could be easily extended with spatio-temporal convolution operations for continuous human motion recognition.
2. **Large Dataset plus Very Deep 3D CNNs:** Another way is to devote to a large dataset and apply common 3D filters to optimize very deep CNNs like ResNet-152[24]. This technology road-map was verified in [77] that utilizes Kinetics dataset[78] (300K videos) and very deep 3D CNNs for action recognition, such as ResNet-200[24], DenseNet-201[25] and ResNeXt-101[79]. Following this road-map, we are considering to build a large dataset. However, comparing to computer vision tasks, WiFi-based human sensing is more complicated because CSI is highly correlated with Tx/Rx deployed surroundings. This correlation would undermine the CSI-Net even being optimized by a very large dataset, once it was to test in a new environment. Thus, de-correlating the CSI with environments is also a significant future work when building large datasets.

8 Conclusion

In this paper, we propose a wireless signal model to analysis CSI variance at the presence of human body. We conclude that human presence even without doing anything can introduce CSI variance, which can has significant potentials for sensing human problems. We elaborately design a unified CNN based networks, named CSI-Net, to handle the CSI data for a variety of sensing human takes. We deploy our system to test the conclusion and CSI-Net on body characterization and activity recognition, including four tasks: biometrics estimation, human identification, hand sign recognition and falling detection. The experimental results show that all tasks can be achieved with distinguished performance. Deserved to be mentioned, our work is the first attempt to propose and achieve biometrics estimation using commodity WiFi devices, which has applicable potentiality on health care. Our work is also one of the earliest attempt to provide empirical understanding of the DNN behaviors in processing CSI data.

Acknowledge

We thank Wei Xi and Kun Zhao for discussion on WiFi properties. We thank Li Zhu, Pan Feng, Zhen Liao, Ziyi Dai and Yang Zi for their helps in data collection. Fei Wang is supported by China Scholarship Council.

References

- [1] Kun Qian, Chenshu Wu, Zimu Zhou, Yue Zheng, Zheng Yang, and Yunhao Liu. Inferring motion direction using commodity wi-fi for interactive exergames. In *Proceedings of the Conference on Human Factors in Computing Systems (CHI)*, pages 1961–1972. ACM, 2017.
- [2] Hong Li, Wei Yang, Jianxin Wang, Yang Xu, and Liusheng Huang. Wifinger: Talk to your smart devices with finger-grained gesture. In *Proceedings of the International Joint Conference on Pervasive and Ubiquitous Computing (UbiComp)*, pages 250–261. ACM, 2016.
- [3] Kamran Ali, Alex X Liu, Wei Wang, and Muhammad Shahzad. Keystroke recognition using wifi signals. In *Proceedings of the Annual International Conference on Mobile Computing and Networking (MobiCom)*, pages 90–102. ACM, 2015.
- [4] Biyi Fang, Nicholas D Lane, Mi Zhang, Aidan Boran, and Fahim Kawsar. Bodyscan: Enabling radio-based sensing on wearable devices for contactless activity and vital sign monitoring. In *Proceedings of the Annual International Conference on Mobile Systems, Applications and Services (MobiSys)*, pages 97–110. ACM, 2016.
- [5] Hao Wang, Daqing Zhang, Yasha Wang, Junyi Ma, Yuxiang Wang, and Shengjie Li. Rt-fall: a real-time and contactless fall detection system with commodity wifi devices. *Transactions on Mobile Computing (TMC)*, 16(2):511–526, 2017.
- [6] Xuyu Wang, Chao Yang, and Shiwen Mao. Tensorbeat: Tensor decomposition for monitoring multi-person breathing beats with commodity wifi. *arXiv preprint arXiv:1702.02046*, 2017.
- [7] Hao Wang, Daqing Zhang, Junyi Ma, Yasha Wang, Yuxiang Wang, Dan Wu, Tao Gu, and Bing Xie. Human respiration detection with commodity wifi devices: Do user location and body orientation matter? In *Proceedings of the International Joint Conference on Pervasive and Ubiquitous Computing (UbiComp)*, pages 25–36. ACM, 2016.
- [8] Wei Xi, Jizhong Zhao, Xiang-Yang Li, Kun Zhao, Shaojie Tang, Xue Liu, and Zhiping Jiang. Electronic frog eye: Counting crowd using wifi. In *Proceedings of the International Conference on Computer Communications (INFOCOM)*, pages 361–369. IEEE, 2014.
- [9] Xiaolong Zheng, Jiliang Wang, Longfei Shangguan, Zimu Zhou, and Yunhao Liu. Smokey: Ubiquitous smoking detection with commercial wifi infrastructures. In *Proceedings of the International Conference on Computer Communications (INFOCOM)*, pages 1–9. IEEE, 2016.
- [10] Fadel Adib and Dina Katabi. See through walls with wifi! In *Proceedings of the SIGCOMM*, pages 75–86. ACM, 2013.
- [11] Sameera Palipana, David Rojas, Piyush Agrawal, and Dirk Pesch. Falldfi: Ubiquitous fall detection using commodity wi-fi devices. *Proceedings of the Interactive, Mobile, Wearable and Ubiquitous Technologies (IMWUT)*, 1(4):155, 2018.
- [12] Heba Abdelnasser, Moustafa Youssef, and Khaled A Harras. Wigest: A ubiquitous wifi-based gesture recognition system. In *Proceedings of the Conference on Computer Communications (INFOCOM)*, pages 1472–1480. IEEE, 2015.

- [13] Heba Abdelnasser, Khaled A Harras, and Moustafa Youssef. Ubibreathe: A ubiquitous non-invasive wifi-based breathing estimator. In *Proceedings of the International Symposium on Mobile Ad Hoc Networking and Computing (MobiHoc)*, pages 277–286. ACM, 2015.
- [14] Sheng Tan and Jie Yang. Wifinger: Leveraging commodity wifi for fine-grained finger gesture recognition. In *Proceedings of the International Symposium on Mobile Ad Hoc Networking and Computing (MobiHoc)*, pages 201–210. ACM, 2016.
- [15] Mengyuan Li, Yan Meng, Junyi Liu, Haojin Zhu, Xiaohui Liang, Yao Liu, and Na Ruan. When csi meets public wifi: Inferring your mobile phone password via wifi signals. In *Proceedings of the Conference on Computer and Communications Security (SIGSAC)*, pages 1068–1079. ACM, 2016.
- [16] Xuyu Wang, Lingjun Gao, Shiwen Mao, and Santosh Pandey. Csi-based fingerprinting for indoor localization: A deep learning approach. *IEEE Transactions on Vehicular Technology*, 66(1):763–776, 2017.
- [17] Cong Shi, Jian Liu, Hongbo Liu, and Yingying Chen. Smart user authentication through actuation of daily activities leveraging wifi-enabled iot. In *Proceedings of the International Symposium on Mobile Ad Hoc Networking and Computing (MobiHoc)*, page 5. ACM, 2017.
- [18] Ross Girshick. Fast r-cnn. *arXiv preprint arXiv:1504.08083*, 2015.
- [19] Shaoqing Ren, Kaiming He, Ross Girshick, and Jian Sun. Faster r-cnn: Towards real-time object detection with region proposal networks. In *Proceedings of Advances in Neural Information Processing Systems (NIPS)*, pages 91–99, 2015.
- [20] Kaiming He, Georgia Gkioxari, Piotr Dollár, and Ross Girshick. Mask r-cnn. In *Proceedings of International Conference on Computer Vision (ICCV)*, pages 2980–2988. IEEE, 2017.
- [21] Alex Krizhevsky, Ilya Sutskever, and Geoffrey E Hinton. Imagenet classification with deep convolutional neural networks. In *Proceedings of the Advances in Neural Information Processing Systems (NIPS)*, pages 1097–1105, 2012.
- [22] Karen Simonyan and Andrew Zisserman. Very deep convolutional networks for large-scale image recognition. *arXiv preprint arXiv:1409.1556*, 2014.
- [23] Christian Szegedy, Wei Liu, Yangqing Jia, Pierre Sermanet, Scott Reed, Dragomir Anguelov, Dumitru Erhan, Vincent Vanhoucke, Andrew Rabinovich, et al. Going deeper with convolutions. In *Proceedings of the Conference on Computer Vision and Pattern Recognition (CVPR)*. IEEE, 2015.
- [24] Kaiming He, Xiangyu Zhang, Shaoqing Ren, and Jian Sun. Deep residual learning for image recognition. In *Proceedings of the Conference on Computer Vision and Pattern Recognition (CVPR)*, pages 770–778, 2016.
- [25] Gao Huang, Zhuang Liu, Kilian Q Weinberger, and Laurens van der Maaten. Densely connected convolutional networks. In *Proceedings of the conference on Computer Vision and Pattern Recognition (CVPR)*, volume 1, page 3. IEEE, 2017.
- [26] Wei Wang, Alex X Liu, and Muhammad Shahzad. Gait recognition using wifi signals. In *Proceedings of the International Joint Conference on Pervasive and Ubiquitous Computing (UbiComp)*, pages 363–373. ACM, 2016.
- [27] Yunze Zeng, Parth H Pathak, and Prasant Mohapatra. Wiwho: Wifi-based person identification in smart spaces. In *Proceedings of the International Conference on Information Processing in Sensor Networks (IPSN)*, page 4. IEEE, 2016.
- [28] Jin Zhang, Bo Wei, Wen Hu, and Salil S Kanhere. Wifi-id: Human identification using wifi signal. In *Proceedings of the International Conference on Distributed Computing in Sensor Systems (DCOSS)*, pages 75–82. IEEE, 2016.
- [29] Tong Xin, Bin Guo, Zhu Wang, Mingyang Li, Zhiwen Yu, and Xingshe Zhou. Freesense: Indoor human identification with wi-fi signals. In *Proceedings of the Global Communications Conference (GLOBECOM)*, pages 1–7. IEEE, 2016.
- [30] Jiguang Lv, Wu Yang, Dapeng Man, Xiaojiang Du, Miao Yu, and Mohsen Guizani. Wii: Device-free passive identity identification via wifi signals. In *Proceedings of the Global Communications Conference (GLOBECOM)*, pages 1–6. IEEE, 2017.
- [31] Qinyi Xu, Yan Chen, BeiBei Wang, and KJ Ray Liu. Radio biometrics: Human recognition through a wall. *Transactions on Information Forensics and Security (TIFS)*, 12(5):1141–1155, 2017.
- [32] Xuefeng Liu, Jiannong Cao, Shaojie Tang, Jiaqi Wen, and Peng Guo. Contactless respiration monitoring via off-the-shelf wifi devices. *Transactions on Mobile Computing (TMC)*, 15(10):2466–2479, 2016.
- [33] Yuxi Wang, Kaishun Wu, and Lionel M Ni. Wifall: Device-free fall detection by wireless networks. *Transactions on Mobile Computing (TMC)*, 16(2):581–594, 2017.

- [34] Donald J Berndt and James Clifford. Using dynamic time warping to find patterns in time series. In *Proceedings of Data Mining and Knowledge Discovery (KDD), Workshop*, volume 10, pages 359–370, 1994.
- [35] Xuyu Wang, Lingjun Gao, Shiwen Mao, and Santosh Pandey. Deepfi: Deep learning for indoor fingerprinting using channel state information. In *Wireless Communications and Networking Conference (WCNC), 2015 IEEE*, pages 1666–1671. IEEE, 2015.
- [36] Xuyu Wang, Lingjun Gao, and Shiwen Mao. Csi phase fingerprinting for indoor localization with a deep learning approach. *IEEE Internet of Things Journal*, 3(6):1113–1123, 2016.
- [37] Xuyu Wang, Lingjun Gao, and Shiwen Mao. Phasefi: Phase fingerprinting for indoor localization with a deep learning approach. In *Global Communications Conference (GLOBECOM), 2015 IEEE*, pages 1–6. IEEE, 2015.
- [38] Hao Ye, Geoffrey Ye Li, and Biing-Hwang Juang. Power of deep learning for channel estimation and signal detection in ofdm systems. *IEEE Wireless Communications Letters*, 7(1):114–117, 2018.
- [39] Jeong-Sik Choi, Woong-Hee Lee, Jae-Hyun Lee, Jong-Ho Lee, and Seong-Cheol Kim. Deep learning based nlos identification with commodity wlan devices. *algorithms*, 1:2, 2017.
- [40] Sepp Hochreiter and Jürgen Schmidhuber. Long short-term memory. *Neural computation*, 9(8):1735–1780, 1997.
- [41] S Gabriel, RW Lau, and Camelia Gabriel. The dielectric properties of biological tissues: Ii. measurements in the frequency range 10 hz to 20 ghz. *Physics in Medicine and Biology*, 41(11):2251, 1996.
- [42] Andreas Christ, Theodoros Samaras, Anja Kligenböck, and Niels Kuster. Characterization of the electromagnetic near-field absorption in layered biological tissue in the frequency range from 30 mhz to 6000 mhz. *Physics in Medicine & Biology*, 51(19):4951, 2006.
- [43] Andreas Christ, Anja Kligenböck, Theodoros Samaras, Cristian Goiceanu, and Niels Kuster. The dependence of electromagnetic far-field absorption on body tissue composition in the frequency range from 300 mhz to 6 ghz. *IEEE transactions on microwave theory and techniques*, 54(5):2188–2195, 2006.
- [44] Ilka Dove. Analysis of radio propagation inside the human body for in-body localization purposes. Master’s thesis, University of Twente, 2014.
- [45] MJ Ackerman and RA Banvard. Imaging outcomes from the national library of medicine’s visible human project®, 2000.
- [46] Bhag Singh Guru and Hüseyin R Hiziroglu. *Electromagnetic field theory fundamentals*. Cambridge university press, 2004.
- [47] Joseph A Shaw. Radiometry and the friis transmission equation. *American Journal of Physics*, 81(1):33–37, 2013.
- [48] Thomas G Mayerhöfer, Harald Mutschke, and Jürgen Popp. Employing theories far beyond their limits—the case of the (boger-) beer–lambert law. *ChemPhysChem*, 17(13):1948–1955, 2016.
- [49] Mi body composition scale. <http://www.mi.com/us/mi-body-composition-scale/>.
- [50] Daniel Halperin, Wenjun Hu, Anmol Sheth, and David Wetherall. Tool release: Gathering 802.11 n traces with channel state information. *SIGCOMM Computer Communication Review*, 41(1):53–53, 2011.
- [51] Yan Yubo, Yang Panlong, Li Xiangyang, Tao Yue, Zhang Lan, and You Lizhao. Zimo: Building cross-technology mimo to harmonize zigbee smog with wifi flash without intervention. In *Proceedings of the Annual International Conference on Mobile Computing and Networking (MiboCom)*, pages 465–476. ACM, 2013.
- [52] Yaxiong Xie, Zhenjiang Li, and Mo Li. Precise power delay profiling with commodity wifi. In *Proceedings of the Annual International Conference on Mobile Computing and Networking (MobiCom)*, pages 53–64. ACM, 2015.
- [53] Shun-ichi Amari, Andrzej Cichocki, and Howard Hua Yang. A new learning algorithm for blind signal separation. In *Advances in neural information processing systems*, pages 757–763, 1996.
- [54] Ian Goodfellow, Jean Pouget-Abadie, Mehdi Mirza, Bing Xu, David Warde-Farley, Sherjil Ozair, Aaron Courville, and Yoshua Bengio. Generative adversarial nets. In *Proceedings of the Advances in Neural Information Processing Systems (NIPS)*, pages 2672–2680, 2014.
- [55] Tim Salimans, Ian Goodfellow, Wojciech Zaremba, Vicki Cheung, Alec Radford, and Xi Chen. Improved techniques for training gans. In *Proceedings of the Advances in Neural Information Processing Systems (NIPS)*, pages 2234–2242, 2016.
- [56] Scott Reed, Zeynep Akata, Xinchun Yan, Lajanugen Logeswaran, Bernt Schiele, and Honglak Lee. Generative adversarial text to image synthesis. *arXiv preprint arXiv:1605.05396*, 2016.
- [57] Emily Denton, Sam Gross, and Rob Fergus. Semi-supervised learning with context-conditional generative adversarial networks. *arXiv preprint arXiv:1611.06430*, 2016.

- [58] Konstantinos Bousmalis, Nathan Silberman, David Dohan, Dumitru Erhan, and Dilip Krishnan. Unsupervised pixel-level domain adaptation with generative adversarial networks. In *Proceedings of the Conference on Computer Vision and Pattern Recognition (CVPR)*, volume 1, page 7. IEEE, 2017.
- [59] Sergey Ioffe and Christian Szegedy. Batch normalization: Accelerating deep network training by reducing internal covariate shift. In *Proceedings of International Conference on Machine Learning (ICML)*, pages 448–456, 2015.
- [60] Christian Szegedy, Vincent Vanhoucke, Sergey Ioffe, Jon Shlens, and Zbigniew Wojna. Rethinking the inception architecture for computer vision. In *Proceedings of the Conference on Computer Vision and Pattern Recognition (CVPR)*, pages 2818–2826. IEEE, 2016.
- [61] Christian Szegedy, Sergey Ioffe, Vincent Vanhoucke, and Alexander A Alemi. Inception-v4, inception-resnet and the impact of residual connections on learning. In *Proceedings of Association for the Advancement of Artificial Intelligence (AAAI)*, volume 4, page 12, 2017.
- [62] Alfredo Canziani, Adam Paszke, and Eugenio Culurciello. An analysis of deep neural network models for practical applications. *arXiv preprint arXiv:1605.07678*, 2016.
- [63] Vinod Nair and Geoffrey E Hinton. Rectified linear units improve restricted boltzmann machines. In *Proceedings of the International Conference on Machine Learning (ICML)*, pages 807–814, 2010.
- [64] Ursula G Kyle, Ingvar Bosaeus, Antonio D De Lorenzo, Paul Deurenberg, Marinos Elia, José Manuel Gómez, Berit Lilienthal Heitmann, Luisa Kent-Smith, Jean-Claude Melchior, Matthias Pirlich, et al. Bioelectrical impedance analysis—part i: Review of principles and methods. *Clinical Nutrition*, 23(5):1226–1243, 2004.
- [65] America sign language. <https://www.graphicsfactory.com/>.
- [66] Diederik P Kingma and Jimmy Ba. Adam: A method for stochastic optimization. *arXiv preprint arXiv:1412.6980*, 2014.
- [67] Chih-Chung Chang and Chih-Jen Lin. LIBSVM: A library for support vector machines. *ACM Transactions on Intelligent Systems and Technology (TIST)*, 2:27:1–27:27, 2011. Software Available at <http://www.csie.ntu.edu.tw/~cjlin/libsvm>.
- [68] David Martin Powers. Evaluation: from precision, recall and f-measure to roc, informedness, markedness and correlation. 2011.
- [69] Jacob Cohen. Statistical power analysis for the behavioral sciences, 2nd edition, 1988.
- [70] Mavuto M Mukaka. A guide to appropriate use of correlation coefficient in medical research. *Malawi Medical Journal*, 24(3):69–71, 2012.
- [71] Alec Radford, Luke Metz, and Soumith Chintala. Unsupervised representation learning with deep convolutional generative adversarial networks. *arXiv preprint arXiv:1511.06434*, 2015.
- [72] Du Tran, Lubomir Bourdev, Rob Fergus, Lorenzo Torresani, and Manohar Paluri. Learning spatiotemporal features with 3d convolutional networks. In *Proceedings of International Conference on Computer Vision (ICCV)*, pages 4489–4497. IEEE, 2015.
- [73] Zheng Shou, Jonathan Chan, Alireza Zareian, Kazuyuki Miyazawa, and Shih-Fu Chang. Cdc: Convolutional-de-convolutional networks for precise temporal action localization in untrimmed videos. In *Proceedings of the Conference on Computer Vision and Pattern Recognition (CVPR)*, pages 1417–1426. IEEE, 2017.
- [74] Ke Yang, Peng Qiao, Dongsheng Li, Shaohe Lv, and Yong Dou. Exploring temporal preservation networks for precise temporal action localization. In *Proceedings of Association for the Advancement of Artificial Intelligence (AAAI)*, 2018.
- [75] Jeffrey Donahue, Lisa Anne Hendricks, Sergio Guadarrama, Marcus Rohrbach, Subhashini Venugopalan, Kate Saenko, and Trevor Darrell. Long-term recurrent convolutional networks for visual recognition and description. In *Proceedings of the Conference on Computer Vision and Pattern Recognition (CVPR)*, pages 2625–2634, 2015.
- [76] Serena Yeung, Olga Russakovsky, Ning Jin, Mykhaylo Andriluka, Greg Mori, and Li Fei-Fei. Every moment counts: Dense detailed labeling of actions in complex videos. *International Journal of Computer Vision (IJCV)*, 126(2-4):375–389, 2018.
- [77] Kensho Hara, Hirokatsu Kataoka, and Yutaka Satoh. Can spatiotemporal 3d cnns retrace the history of 2d cnns and imagenet? *arXiv preprint arXiv:1711.09577*, 2017.
- [78] Will Kay, Joao Carreira, Karen Simonyan, Brian Zhang, Chloe Hillier, Sudheendra Vijayanarasimhan, Fabio Viola, Tim Green, Trevor Back, Paul Natsev, et al. The kinetics human action video dataset. *arXiv preprint arXiv:1705.06950*, 2017.

[79] Saining Xie, Ross Girshick, Piotr Dollár, Zhuowen Tu, and Kaiming He. Aggregated residual transformations for deep neural networks. In *Proceedings of the Conference on Computer Vision and Pattern Recognition (CVPR)*, pages 5987–5995. IEEE, 2017.

9 Appendix

9.1 Technical Details of SVM

A CSI data instance is considered as a tensor with size of $30 \times 1 \times 1$ (channel of 30, width of 1 and height of 1) in CSI-Net it can also be considered as a vector with size of 30, which means each instance has 30-d features. We donate one CSI instance as $x \in R^{30}$, and donate $x_{(k)}$ as the k -th features of x .

With the guidebook of LibSVM[67], we first normalize training dataset to the value within $[-1, +1]$ as following equation.

$$x'_{(k)} = 2 \times \frac{x_{(k)} - X_{(k)}^{min}}{X_{(k)}^{max} - X_{(k)}^{min}} - 1, k \in [1, 2, \dots, 30] \quad (9)$$

where $X_{(k)}^{max}$ and $X_{(k)}^{min}$ is the maximum and minimum of the k -th features in all training instances respectively, $x'_{(k)}$ is the k -th feature of a normalized instance.

Then we utilize the maximum ($X_{(k)}^{max}$) and minimum ($X_{(k)}^{min}$) in training dataset to normalize test instances with following equation.

$$x^*_{(k)} = 2 \times \frac{x_{(k)} - X_{(k)}^{min}}{X_{(k)}^{max} - X_{(k)}^{min}} - 1, k \in [1, 2, \dots, 30] \quad (10)$$

where the $x_{(k)}$ and $x^*_{(k)}$ is the original and normalized k -th feature of one test instance, respectively. The above normalization is a very practical operation when applying LibSVM, it increases the human identification accuracy from 25.08% to 85.28% for our dataset.

We formalize the SVM classifier with notation of $y = w^T x + b$, where x is the data instance, w and b are *weights* and *bias* of the classifier, and the y is the prediction output. We apply L2 regularization to constrain the model complexity, and set penalty parameter as 1 to punish the model for its misclassifying. Then the *loss* function of SVM can be **simply formalized** as follows.

$$L = \sum_{i=1}^m D(y^i, w^T x^i + b) + \frac{1}{2} w^T w + C \sum_{j=1}^N \mathbb{I}(y^j, w^T x^j + b) \quad (11)$$

where $D(y^i, w^T x^i + b)$ is to compute the distance between the prediction of x^i ($(w^T x^i + b)$) and the real value(y^i), m is the number of support vectors. The part of $\frac{1}{2} w^T w$ is the L2 regularization. The $\mathbb{I}(y^j, w^T x^j + b)$ is an indicator with value of 0/1 for right/not right prediction, those misclassified instances will increase the *loss* according to $C \sum_{j=1}^N \mathbb{I}(y^j, w^T x^j + b)$, where C is the penalty parameter and was set to 1, N is the number of training instances.

We use radius basis function (RBF) kernel showed below to map instance to a non-linear space.

$$K(x^i, x^j) = e^{-\frac{(x^i - x^j)^2}{30}} \quad (12)$$

Finally we use the one-against-all strategy to solve multi-class classification problems such as identifying 30 subjects and recognizing 10 hand signs. The one-against-all strategy will learn c classifiers if the number of class is c . When learning the k -th classifier, it considers the instances those belongs to the k -th class as *class one*, considers all remaining instances as *class two*, so every classifier is learned for a binary classification problem. The prediction category (p) is the index of a classifier that produces the maximal score for an instance among all classifiers, which shown in Eq. 13.

$$p = \arg \max_{i \in \{1, 2, \dots, k\}} w_{(i)}^T x + b_{(i)} \quad (13)$$

9.2 Technical Details of Naïve Bayes

The inputs of CSI-Net are with size of $30 \times 1 \times 1$, which are considered instances with 30 features, $x \in R^{30}$, at the implementation of Naïve Bayes.

To classify a test instance, x' , we can compute the probability of that belongs to the k -th class, $p(k|x')$, with Bayes Rule as following equation.

$$p(k|x') = \frac{p(x'|k) \times p(k)}{p(x')} \quad (14)$$

where $p(x'|k)$ is the appearing probability of x' knowing that x' belongs to the k -th class, $p(k)$ and $p(x')$ is the appearing probability of k -th class and x' respectively.

Supposing that all classes appear with the same probability, the $p(k)$ can be neglected. Meanwhile, though we can not obtain $p(x')$, it is will divided by $p(x'|k)$, which means $p(x')$ can also be neglected. So computing $p(k|x')$ can be achieved by computing $p(x'|k)$.

$$p(k|x') = \frac{p(x'|k) \times p(k)}{p(x')} \propto p(x'|k) \quad (15)$$

Supposing that all 30 features of x are independent with each other, $p(x'|k)$ can be calculated by following equation.

$$p(k|x') \propto p(x'|k) = \prod_{i=1}^{30} p(x'_i|k) \quad (16)$$

where x'_i is the i -th feature of instance x' , $p(x'_i|k)$ is appearing probability of x'_i knowing that it belong to the k -th class.

Supposing that features of CSI instances follow Gaussian distribution, we first calculate the mean and square deviation of every feature of the k -th class using training data. The X_i stands for the i -th feature of all training data, $\mu(X_i|k)$ represents the mean of the i -th feature among training data with label of k -th class, and $\sigma^2(X_i|k)$ is for the is the square deviation of i -th feature among training data with label of k -th class.

Then we use probability density function of Gaussian Distribution to compute $p(x'_i|k)$.

$$p(x'_i|k) = \frac{1}{\sqrt{2\pi\sigma^2(X_i|k)}} e^{-\frac{(x'_i - \mu(X_i|k))^2}{2\sigma^2(X_i|k)}} \quad (17)$$

After obtaining $p(x'_i|k)$, we compute the probability of $p(x'|k)$ by Eq. 16. And we will compute all $p(x'|k)$, $k \in [1, 2, \dots, C]$, where C is the number of classes. Finally, the prediction is the class of k^* that with maximal value among all $p(x'|k)$, $k \in [1, 2, \dots, C]$.

9.3 Detailed CSI-Net Parameters

layer name	layer parameters	output size
transposedconv_1	$4 \times 4, 384, \text{stride}=2, \text{padding}=1$	$384 \times 2 \times 2$
transposedconv_2	$4 \times 4, 192, \text{stride}=2, \text{padding}=1$	$192 \times 4 \times 4$
transposedconv_3	$3 \times 3, 96, \text{stride}=2, \text{padding}=1$	$96 \times 7 \times 7$
transposedconv_4	$4 \times 4, 48, \text{stride}=2, \text{padding}=1$	$48 \times 14 \times 14$
transposedconv_5	$4 \times 4, 24, \text{stride}=2, \text{padding}=1$	$24 \times 28 \times 28$
transposedconv_6	$4 \times 4, 12, \text{stride}=2, \text{padding}=1$	$12 \times 56 \times 56$
transposedconv_7	$4 \times 4, 6, \text{stride}=2, \text{padding}=1$	$6 \times 112 \times 112$
transposedconv_8	$4 \times 4, 6, \text{stride}=2, \text{padding}=1$	$6 \times 224 \times 224$
conv1	$7 \times 7, 64, \text{stride}=2, \text{padding}=3$	$64 \times 112 \times 112$
max_pool	$3 \times 3, \text{stride}=2, \text{padding}=1$	$64 \times 56 \times 56$
conv2_x	$\begin{bmatrix} 3 \times 3, & 64 \\ 3 \times 3, & 64 \end{bmatrix} \times 2$	$64 \times 56 \times 56$
conv3_x	$\begin{bmatrix} 3 \times 3, & 128 \\ 3 \times 3, & 128 \end{bmatrix} \times 2$	$128 \times 28 \times 28$
conv4_x	$\begin{bmatrix} 3 \times 3, & 256 \\ 3 \times 3, & 256 \end{bmatrix} \times 2$	$256 \times 14 \times 14$
conv5_x	$\begin{bmatrix} 3 \times 3, & 512 \\ 3 \times 3, & 512 \end{bmatrix} \times 2$	$512 \times 7 \times 7$

Table 15: Shared layers of all tasks. These layers consist of generation stage from layer of transposedconv_1 to layer of transposedconv_8 and part of feature learning stage from layer conv1 to layer of conv5_x. The layers of generation stage generate data with size of $6 \times 224 \times 224$. The following feature learning layers are part of ResNet-18[24] and produce data with size of $512 \times 7 \times 7$, which later is fed to the branch that belongs to each specific task.

layer name	layer parameters	output size
conv_6	$3 \times 3, 512, \text{stride}=2, \text{padding}=1$	$512 \times 4 \times 4$
conv_7	$4 \times 4, 256, \text{stride}=2, \text{padding}=1$	$256 \times 2 \times 2$
ave_pool	$2 \times 2, \text{padding}=0$	256
fc	4-d fc, relu, L1	4

Table 16: Biometrics estimation branch. This branch is paralleled with Human Identification Branch showed in Table 17, and follows at the end of conv5_x in Table 15. This branch is composed of 2 *convolution* layers, 1 *average pool* layer and 1 *fully-connected* layer. Because we are to estimate 4 biometrics, we set the dimension of output 4.

layer name	layer parameters	output size
conv_6	$3 \times 3, 512, \text{stride}=2, \text{padding}=1$	$512 \times 4 \times 4$
conv_7	$4 \times 4, 256, \text{stride}=2, \text{padding}=1$	$256 \times 2 \times 2$
ave_pool	$2 \times 2, \text{padding}=0$	256
fc	30-d fc, softmax, cross entropy	30

Table 17: Human identification branch. This branch parallels with biometrics estimation branch showed in Table 16, and follows at the end of conv5_x in Table 15. This branch is composed of 2 *convolution* layer, 1 *average pool* and 1 *fully-connected* layer. Because we are to identify 30 subjects, we set the dimension of output 30.

layer name	layer parameters	output size
conv_6	$3 \times 3, 256, \text{stride}=2, \text{padding}=1$	$256 \times 4 \times 4$
conv_7	$4 \times 4, 128, \text{stride}=2, \text{padding}=1$	$128 \times 2 \times 2$
ave_pool	$2 \times 2, \text{padding}=0$	128
fc	10-d fc, softmax, cross entropy	10

Table 18: Sign recognition branch. The shared layers showed in Table 15 and layers in this branch form a CSI-Nethat used for recognizing human finger sign. This branch consists of 2 *convolution* layer, 1 *average pool* and 1 *fully-connected* layer. Because we are to recognize 10 hand signs (from number 0 to number 9), we set the dimension of output 10. Comparing to the branch for biometrics estimation and human identification, we reducing the output size of each layer for avoiding overfitting is because we consider the complexity of this task is lower than the above.

layer name	layer parameters	output size
conv_6	$3 \times 3, 256, \text{stride}=2, \text{padding}=1$	$256 \times 4 \times 4$
conv_7	$4 \times 4, 128, \text{stride}=2, \text{padding}=1$	$128 \times 2 \times 2$
ave_pool	$2 \times 2, \text{padding}=0$	128
fc	2-d fc, softmax, cross entropy	2

Table 19: Falling detection branch. The shared layers showed in Table 15 and layers in this branch form a CSI-Net that used for detecting human falling. This branch consists of 2 *convolution* layer, 1 *average pool* and 1 *fully-connected* layer. Because we are to detect a human falling or not, we set the dimension of output 2. Comparing to the branch for biometrics estimation and human identification, we reducing the output size of each layer for avoiding overfitting is because we consider the complexity of this task is lower than the above.

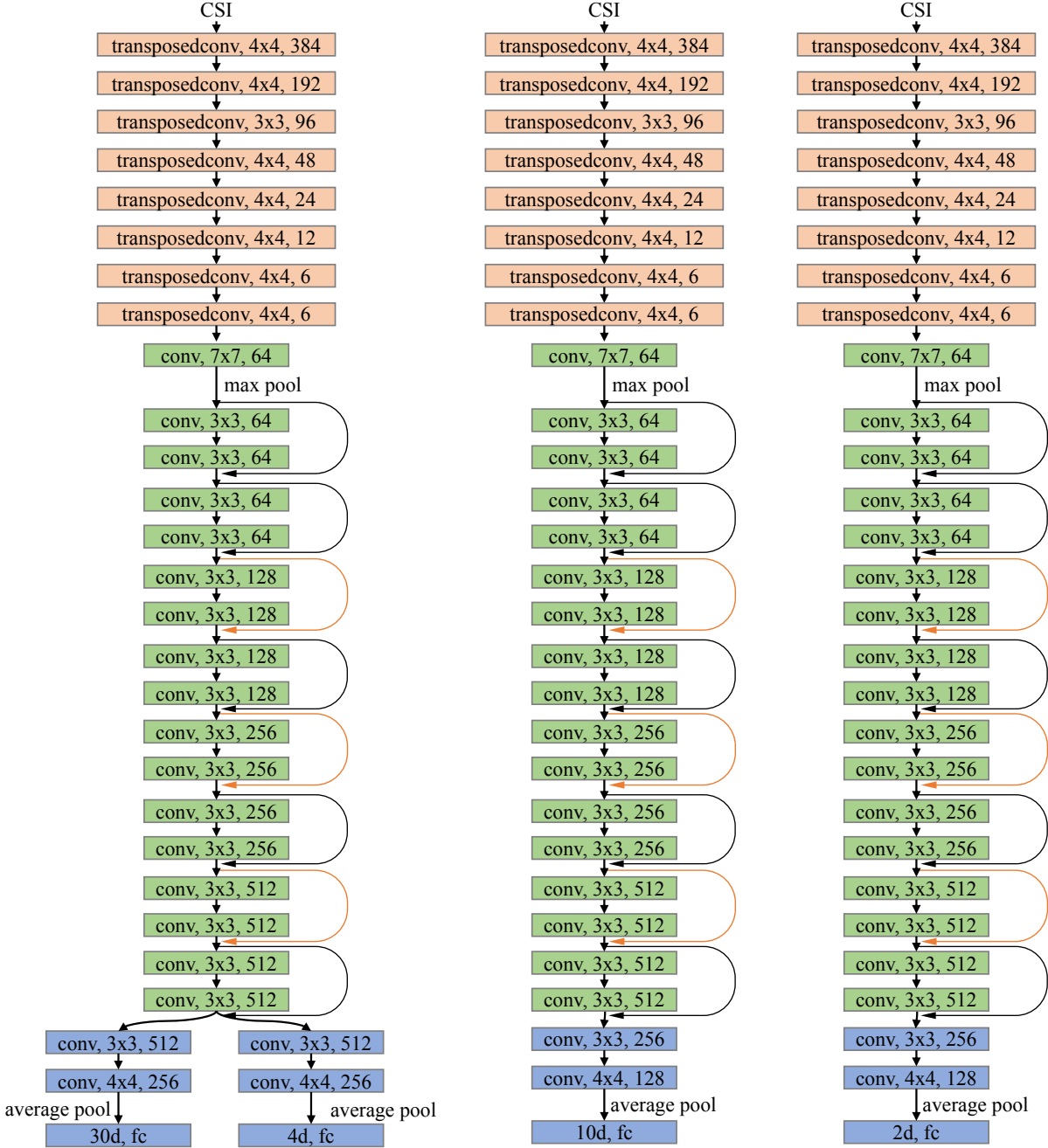


Figure 13: Sketches of CSI-Net architectures for tasks of, **Left**: joint biometrics estimation and human identification, **Middle**: hand sign recognition, and **Right**: falling detection. The orange shortcuts increase channels.

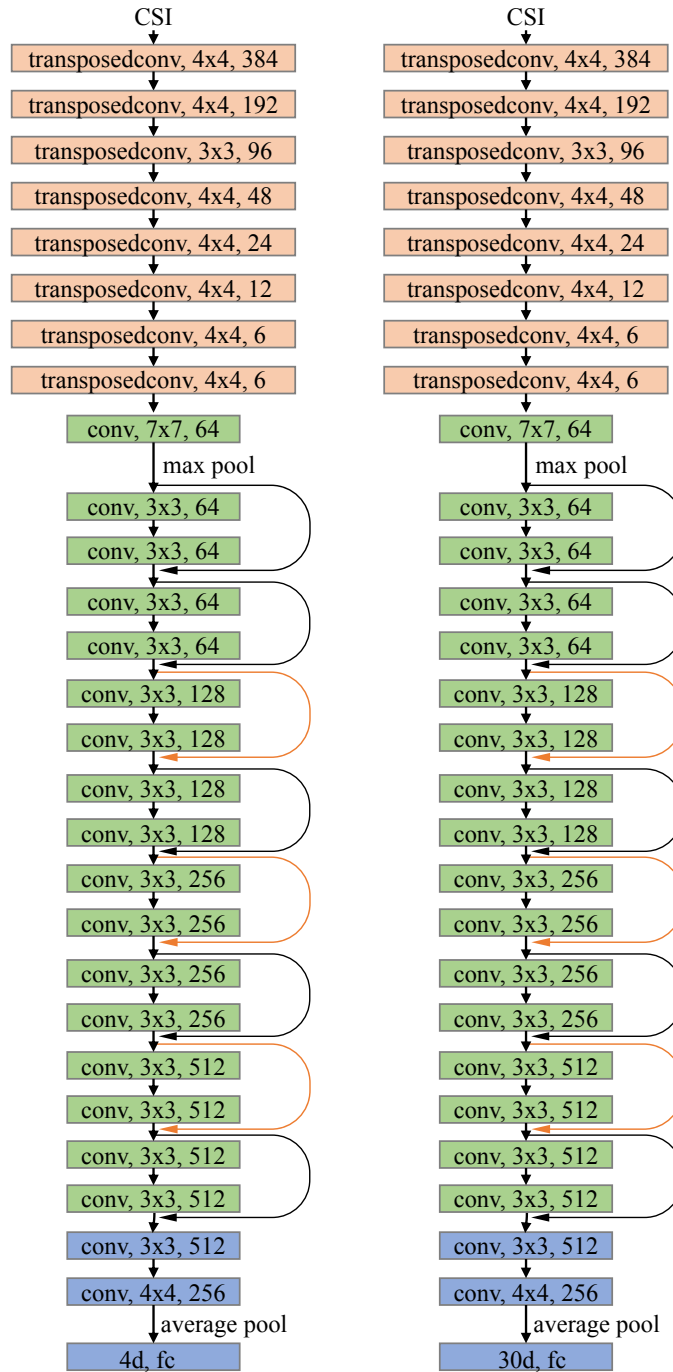


Figure 14: Sketches of CSI-Net architectures for separately-trained tasks of, **Left**: biometrics estimation, and **Right**: human identification